Space Weather

RESEARCH ARTICLE
10.1029/2023SW003502

Ionospheric Disturbances Generated by the 2015 Calbuco Eruption: Comparison of GITM-R Simulations and GNSS Observations

J. Tyska[1], Y. Deng[1], S. Zhang[2], and C. Y. Lin[3]

[1]University of Texas at Arlington, Arlington, TX, USA, [2]Massachusetts Institute of Technology Haystack Observatory, Westford, MA, USA, [3]National Central University, Taoyuan, Taiwan

Key Points:

- GNSS TEC data analysis for the first phase of the 2015 Calbuco eruption shows varied acoustic (A) and gravity (G) dominant perturbations
- A simplified source representation and spectral A-G wave model are used to drive GITM-R to capture meso-scale perturbations near the source
- The relative amplitude and phase speeds of acoustic and gravity wave driven ionospheric disturbance are reproduced in GITM-R simulations

Correspondence to:
Y. Deng,
yuedeng@uta.edu

Citation:
Tyska, J., Deng, Y., Zhang, S., & Lin, C. Y. (2024). Ionospheric disturbances generated by the 2015 Calbuco eruption: Comparison of GITM-R simulations and GNSS observations. *Space Weather*, *22*, e2023SW003502. https://doi.org/10.1029/2023SW003502

Received 27 MAR 2023
Accepted 11 JAN 2024

Abstract Volcanic eruptions provide broad spectral forcing to the atmosphere and understanding the primary mechanisms that are relevant to explain the variety in waveform characteristics in the Ionosphere-Thermosphere (IT) is still an important open question for the community. In this study, Global Navigation Satellite System (GNSS) Total Electron Content (TEC) data are analyzed and compared to simulations performed by the Global Ionosphere-Thermosphere Model with Local Mesh Refinement (GITM-R) for the first phase of the 2015 Calbuco eruption that occurred on 22 April. A simplified source representation and spectral acoustic-gravity wave (AGW) propagation model are used to specify the perturbation at the lower boundary of GITM-R at 100 km altitude. Two assumptions on the propagation structure, Direct Spherical (DS) and Ground Coupled (GC), are compared to the GNSS data and these modeling specifications show good agreement with different aspects of the observations for some waveform characteristics. Most notably, GITM-R is able to reproduce the relative wave amplitude of AGWs as a function of radial distance from the vent, showing acoustic dominant forcing in the near field (<500 km) and gravity dominant forcing in the far-field (>500 km). The estimated apparent phase speeds from GITM-R simulations are consistent with observations with ∼10% difference from observation for both acoustic wave packets and a trailing gravity mode. The relevance of the simplifications made in the lower atmosphere to the simulated IT response is then discussed.

Plain Language Summary The two eruption phases of the 2015 Calbuco volcanic event created atmospheric pressure and gravity disturbances that were measured as plasma disturbances in the earth's upper atmosphere by global navigation satellites. This study utilizes a fully self-consistent global circulation model of the upper atmosphere, with a highly flexible resolution, to simulate and investigate our understanding of the coupled atmosphere-plasma system in the event of a volcanic eruption. It is shown that the current methodology is capable of recreating important features of the observed upper atmospheric signals which include magnitude distributions, arrival times, and the relative contributions of pressure and gravity influenced waves as a function of distance from the volcano.

1. Introduction

It is known that explosive events can generate acoustic-gravity waves (AGWs) that propagate, by virtue of the atmosphere's density profile, to thermospheric heights and influence the ionosphere in a way detectable by dual frequency Global Navigation Satellite Systems (GNSS) (Calais et al., 1998; Cheng & Huang, 1992; Hines, 1960; C. Y. Huang et al., 2019; Klobuchar, 1985; Komjathy et al., 2012; Koucká Knížová et al., 2021). Kanamori et al. (1994) demonstrated that point source forcing in an isothermal atmosphere, depicting injection of mass/energy, resulted in two dominant modes, one below the buoyant frequency and the other above the acoustic cut-off frequency. It had been shown previously from C. H. Liu and Yeh (1971) and Chimonas and Hines (1970) that the far field response of relatively localized sources is influenced by the buoyant, gravity, and acoustic modes, suggesting that these frequencies may explain some of the dominant structures present in the Ionosphere-Thermosphere (IT) system as a direct consequence of a volcanic eruption.

Progress in observational capabilities, primarily advances in GNSS infrastructure, have allowed for a variety of Covolcanic Ionospheric Disturbance(s) (CVIDs) to be detected and analyzed. The extraordinary Tonga event has generated additional interest in the IT response to volcanic eruptions because of local and global affects that are of explanatory value to the community (L. Liu et al., 2023; Themens et al., 2022; K. Zhang et al., 2022; S.-R. Zhang, Nishimura, et al., 2022; Zhang, Vierinen, et al., 2022). A few examples include the horizontally broad

ionospheric hole that persisted ∼16 hr after the eruption (Aa, Zhang, Erickson, et al., 2022; Aa, Zhang, Wang, et al., 2022; He et al., 2023), suppression and X-pattern merging of the equatorial ionization anomaly (Aa, Zhang, Erickson, et al., 2022; Aa, Zhang, Wang, et al., 2022; K. Zhang et al., 2022), the modification of electric field systems (Harding et al., 2022), and the upper atmospheric manifestation of surface waves, such as the Lamb wave (LW), (cited in most above; Matoza et al., 2022; Vadas, Becker, et al., 2023; Vadas, Figueiredo, et al., 2023). The unprecedented data coverage from a variety of instruments allows for an attempt at a cohesive understanding of energy redistribution in the coupled lithosphere-ocean-atmosphere-ionosphere-magnetosphere system, however such coverage should be supplemented with detailed modeling to infer causal links between observed CVIDs and known physical processes.

CVIDs observed following main eruption phases are typically categorized as one of two types in the measured total electron content (TEC) signals (Cahyadi et al., 2021). Thought to be indicative of the eruption dynamics, the first type (T1) consists of N-shaped pulses and are associated with acoustic/shock perturbations created by sudden, sufficiently intense, explosions like a vulcanian eruption (and similarly, manmade explosions). The second type (T2) is thought to be associated with a continuous eruption style, such as Plinian or sub-Plinian eruptions, and comes in the form of Quasi-periodic TEC oscillations with dominant AGW modes (Astafyeva, 2019; Cahyadi et al., 2020). As a result, T1 disturbances often arrive in the IT system in ∼8–12 min, roughly corresponding to propagation at the sound speed, while T2 disturbances can take anywhere from ∼14 to 60 min. Because of source variability (size, intensity, duration, etc.), the TEC data associated with CVIDs show a variety of waveform characteristics with typical magnitudes often of the order ∼0.1–0.9 TECU and apparent phase speeds ranging from ∼100 to 1,000+ m/s. (Astafyeva et al., 2022; Cahyadi et al., 2020; Dautermann, Calais, Lognonné, & Mattioli, 2009; Heki, 2006; Manta et al., 2021; Nakashima et al., 2016; Shults et al., 2016; Yue et al., 2022; S.-R. Zhang, Nishimura, et al., 2022; Zhang, Vierinen, et al., 2022; K. Zhang et al., 2022). However, several authors have stressed the use of a relative measure for proper feature extraction, or comparisons, as observational TEC waveforms are also heavily influenced by the local geomagnetic field orientation, background ionospheric conditions, and line of sight (LOS) satellite-receiver geometry (Bagiya, et al., 2019; Cahyadi et al., 2020; Calais et al., 1998; Heki & Ping, 2005; Inchin, 2020; Zettergren & Snively, 2015).

The spectral content of the ionospheric response is mostly acoustic dominant with spectral peaks typically cited around the acoustic-cutoff frequency of the neutral atmosphere (∼3.6–3.8 mHz). Gravity dominant wave modes are not always present in the TEC data during a volcanic eruption, but several studies have documented disturbances with dominant peaks at 1–2 mHz (Lindstrom, 2015; Yue et al., 2022). Additionally, theory and observational evidence from mesospheric airglow and satellite images indicate the generation of gravity waves (GWs) from volcanic eruptions should not be neglected (Cappucci, 2021; Miller et al., 2015).

Although observational evidence for CVIDs is quite pronounced, attempts to simulate these events have been infrequent. Most methodologies use ray tracing of a simplified forcing function and consider ionospheric dynamics by utilizing the momentum and continuity equations for an assumed electron density distribution (Dautermann, Calais, Lognonné, & Mattioli, 2009; Heki, 2006; Heki & Fujimoto, 2022). These methodologies have shown good agreement with fitting N-shaped TEC variations to N-shaped forcing functions. Using a similar approach, Dautermann, Calais, Lognonné, and Mattioli (2009) showed the importance of AGW dispersion in explaining the observed acoustic wave trains and later considered the eigenmodes of a coupled earth-atmosphere model to drive the ionospheric disturbances (Dautermann, Calais, & Mattioli, 2009). Their results showed that both measurements in the earth and GPS-TEC signals could be explained by a single explosive atmospheric source and the observed wave packets in the IT system are a consequence of the superposition of the three least attenuated modes. Zettergren and Snively (2015) were the first to use a two-dimensional (2D) compressible atmospheric model in conjunction with a multi-species 2D ionospheric model to investigate plasma responses to volcano like forcing, albeit under the guise of a generalized forcing function for natural hazards. Nevertheless, the dominant predicted acoustic periods match well to that of analyzed CVID events and their simulations showed quantitatively how the source characteristics and local geomagnetic field orientation influence the ionospheric response.

While lots of progress has been made to understand the IT disturbance caused by geographic events through both observations and modeling, understanding the primary mechanisms that are relevant to explain the variety of waveform characteristics found in the system is still an important open question for the community. The current literature on simulated CVIDs is lacking in two key areas. First, the ray tracing methodologies all assume some simplified form of the complex coupling occurring in the IT system and this comes at the price of self-consistency

when compared to a full IT model. Second, the previous attempts are mostly constrained to 2D local domains and as such not only limit the dynamics but may interfere with the background state through impositions of the regional boundary conditions. In this study, we utilize the newly developed Global ionosphere-thermosphere model with local mesh refinement (GITM-R, Deng et al., 2021) to simulate the first phase of the 2015 Calbuco eruption. The propagation of a simplified forcing function is used for the domain below 100 km altitude, but in this study a fully self-consistent model for IT coupling is utilized to calculate the ionospheric response and for the first time simulate high resolution meso-scale CVIDs in a global circulation model (GCM), made possible by the local mesh refinement feature. The data-model comparison shows that the observed propagation speed and perturbation amplitude have been well reproduced by the GITM-R simulations. The relative significance of acoustic wave and gravity wave and its dependence on the distance from the eruption location have been examined through both observations and modeling. Meanwhile, some preliminary study indicates that including the ground-coupling process can be a promising way to further improve the data-model comparison in the future.

2. Calbuco 2015 Event and Previous Observations

The Calbuco volcano is located at ~ 41.3°S, 72.6°W in Southern Chile near the west coast and its vent is approximately 2 km above sea level (Matoza et al., 2018). On 22–23 April 2015, Calbuco erupted following brief seismic activity (<3 hr prior) with two main sub-Plinian phases. The first eruption phase began on April 22nd at 21:04 UT (18:04 LT) and lasted approximately 1.5 hr based on seismic and visual records. After a nearly 5.5-hr pause, the second eruption phase started on April 23rd at 4:00 UT (1:00 LT) and continued for 6 hr (Castruccio et al., 2016; Matoza et al., 2018). Both phases were categorized as 4, out of 8, on the Volcanic Explosivity Index (VEI), which is in the range typically associated with CVID detection (Astafyeva, 2019). Fall deposit and umbrella expansion methods roughly predict bulk injected volumes in the range ~0.27–0.56 km^3, with ~15% being attributed to the first phase and ~85% the second phase (Castruccio et al., 2016; Van Eaton et al., 2016). Although the second phase was continuous, a notable change in the eruption dynamics occurred ~2 hr after the phase start time. The release of pyroclastic density currents from the vent resulted in a decrease in the eruption rate, and associated plume height, while increasing the electrical activity (Castruccio et al., 2016; Van Eaton et al., 2016). The eruptive column eventually returned to its original height until its abrupt end at ~10:00 UT. It is interesting to note the difference between the dynamics and duration of the lower atmospheric response, lasting ~1.5 for the first phase and ~5.5 hr for the second phase, while each ionospheric response only seemed to last ~1.5 hr and had similar waveform characteristics (X. Liu et al., 2017; Shults et al., 2016).

The ionospheric disturbances induced by the eruptive phases have been analyzed previously and the CVIDs were examined by filtering the TEC time series using a bandpass fourth-order zero-phase butter-worth filter with a lower cutoff frequency of 3 mHz and higher cutoff frequencies of 8 and 10 mHz, respectively (X. Liu et al., 2017; Shults et al., 2016). Although they used data from different networks, both showed agreeable results with documented filtered TEC magnitudes of 0.4–0.6 TECU for the first eruption phase and 0.1–0.3 TECU for the second (X. Liu et al., 2017; Shults et al., 2016). X. Liu et al. (2017) estimates the apparent phase speeds as ~800 and ~900 m/s for each respective eruption phase while Shults et al. (2016) estimates ~900 m/s for the first eruptive phase and ~1,100–1,300 m/s for the second. These discrepancies may be caused by the differences in the corresponding data sets, such as LOS geometry and its relation to CVID wave fronts, or perhaps a methodological contrast when making assumptions about the F2 peak height used in calculations. Both studies report similar spectral content with independent analysis confirming spectral dominance at ~3.7 mHz in X. Liu et al. (2017) and 3.8–5.2 mHz in Shults et al. (2016); reasoning these peaks occur due to the superposition of eigenmodes in the coupled earth atmosphere system as in Dautermann, Calais, and Mattioli (2009).

This study focuses on the first eruption phase since the initial atmospheric state better represents the traditional climatology, whereas propagation of AGWs in the second eruptive phase may be influenced by the first.

3. Methodology

This section starts with Section 3.1 that describes the analyzed GNSS TEC data produced by the MIT Haystack Observatory using global GNSS TEC receiver networks for both phases of the 2015 Calbuco eruption. Section 3.2 describes the specific version of (the) Global Ionosphere Thermosphere Model (GITM) used in simulating the ionospheric response to the first eruption phase. Section 3.3 describes how the forcing is applied to GITM's lower boundary in the case of Direct Spherical (DS) propagation and Ground Coupled (GC) propagation.

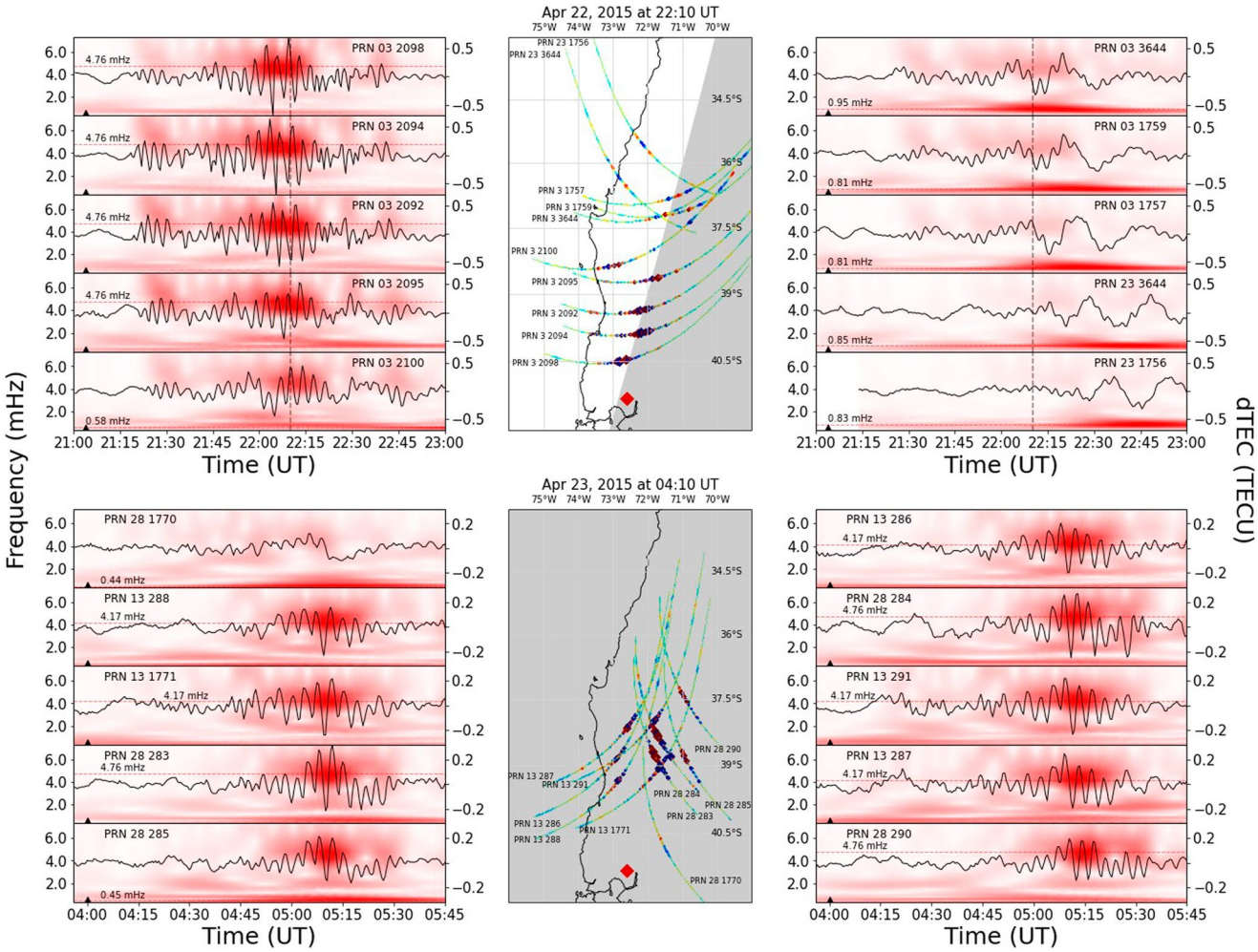

Figure 1. Detrended TEC data for the first (top row) and second (bottom row) eruption phase; measured by the right axis. The background contour represents the corresponding wavelet transform of the displayed time series; measured by the left axis. The dashed red line represents the frequency with maximum transform amplitude in the time series. The middle panels display estimated IPP trajectories for the GNSS observations as well as the volcano location (red diamond). The black triangle along the time axis represents the start time of the eruption for each respective phase while the dashed black line corresponds to the UT associated with the terminator line shown in the middle panel (first phase only).

3.1. Overview of MIT GNSS Observations

This study focuses attention on measurements north (N) and northeast (NE) of the volcano due to limited data availability poleward of the volcano. The GNSS TEC data are converted to dTEC by subtracting a smoothed version of the signal using a Savitzky-Golay 1D filter with a window length of 30 min (Virtanen et al., 2020). This Savitzky-Golay filter detrending approach is extensively used to derive TID information; detailed information can be found in for example, S.-R. Zhang et al. (2017). This window allows for effective TID detection without contamination by large scale ionospheric structures. The left and right panels of Figure 1 show the detrended GNSS TEC variations for a few of the satellite-receiver (PRN #-site #) pairs in both eruption phases. The top row of figures is for the first phase while the bottom row of figures is for the second. The *X*-axis shows the UT time and the *Y*-axis (right) of each of the four data panels shows the amplitude of the detrended GNSS TEC data in TECU (1 TECU $\sim 10^{16}$ electrons/m^2). The background contour displays the wavelet transform of the times series and provides spectral information as a function of time, measured by *Y*-axis (left) in mHz. The wavelet transform is performed utilizing the python *pywt* package (Lee et al., 2019) and a complex Morlet wavelet is used for the transform. Figure 1 is oriented such that distance of the GNSS observations from the volcano increases from top to bottom for each of the four data panels. We define the distance of an observation for a satellite-receiver pair by calculating the horizontal distance from the volcanos vent and the position along the ionospheric piercing point

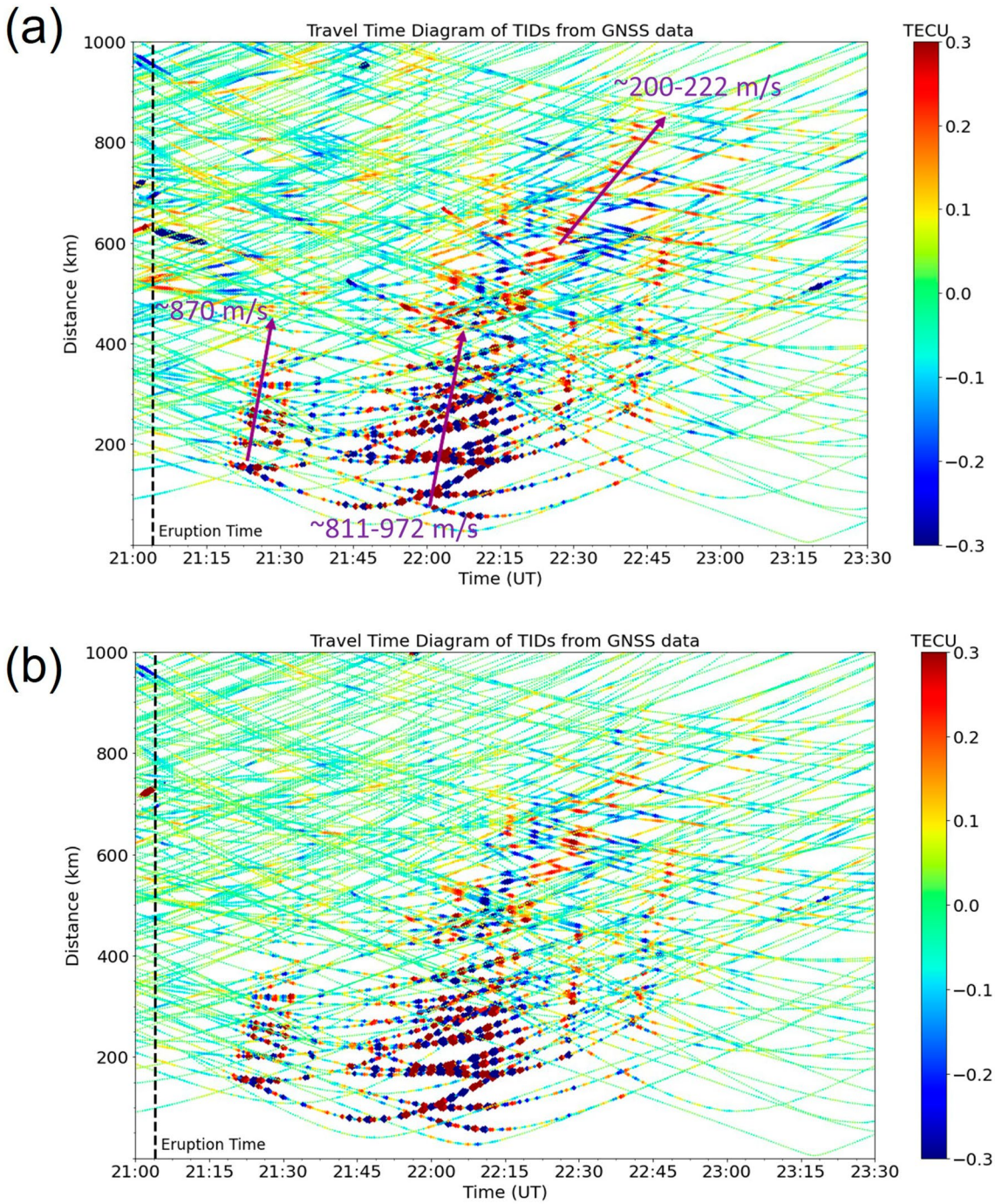

Figure 2. Travel time diagrams (TTD) for GNSS TEC observations following the first eruption phase. (a) 30-min SG filter. (b) 15-min SG filter. Dot size is proportional to TECU magnitude, and the color bar is oversaturated to enhance wave visibility.

(IPP) trajectory where the maximum detrended TECu occurs. For the first eruption phase, the left panel consists of near and mid-field observations (<500 km from the source) and the right panel consists of far-field observations (>500 km from the source); however, for the second eruption phase most observations are in the mid-field. The near (<400 km), mid (400–500 km), and far (>500 km) fields are defined, for this event, by the apparent transition of dominant CVID modes inferred from the full travel time diagram (TTD) for the first eruption phase (see Figure 2). The middle panels provide a spatial supplement for the observations showing oversaturated data along the IPP trajectories for the individual PRN-site pairs. We assume an ionospheric shell height at 300 km for IPP estimation.

Figure 2 shows the TTD for the GNSS data during the first eruption phase. The only difference between (a) and (b) is the duration of the SG sliding filter, where (a) is 30 min and (b) is 15 min. Visible near the source (<400 km) are the high frequency variations associated with the first and second wave packets while a lower frequency mode starts to dominate in the far field (>500 km).

3.2. Global Ionosphere-Thermosphere Model With Local-Mesh Refinement (GITM-R)

GITM is a 3D non-hydrostatic GCM that solves the Navier-stokes equations for the neutral constituents and simplified dynamics for the plasma constituents, however it does not solve for magnetic fields or currents (Deng et al., 2008; Ridley et al., 2006). GITM uses a stretched altitudinal coordinate with discretization dependent on the scale height (~H/3 in this study) and utilizes two-dimensional domain decomposition that allows for flexibility in specifying the meridional and zonal resolutions. The newly developed version with local-mesh refinement feature (GITM-R) increases this flexibility by allowing layered patches of increased resolution to be embedded and coupled together (Deng et al., 2021; Zhao et al., 2020). The advantages of using GITM-R for localized meso-scale AGW simulations are threefold:

(1) The grid refinement using regional patches allow for extreme flexibility in specifying the resolution in areas of interest. The patches are imbedded into a global grid and can be 2-way coupling so that regional boundary conditions can be more realistically set (Deng et al., 2021).
(2) GITM-R has a self-consistent physics-based description of the coupling between the IT system and solves for neutral and ion densities, dynamics, and temperatures. It includes chemistry, solar and geomagnetic inputs, and viscous and thermal conduction terms for more accurate descriptions of IT phenomena (Meng et al., 2022; Ridley et al., 2006).
(3) GITM's numerical configuration allows for non-hydrostatic solutions by explicitly solving the vertical momentum equation. This permits the upward propagation of acoustic waves and gives a more complete description of high frequency AGWs (Deng & Ridley, 2014; Deng et al., 2008).

For this simulation a 3-layer embedded configuration is used and partially shown in Figure 3. The innermost regional layer is centered at the volcano location (41.3°S, 72.6°W) and spans ~15° (~1,500 km) in either horizontal direction creating a 30° × 30° domain with 0.1° × 0.1° resolution. The second regional domain spans a 60° × 60° square centered at the volcano location and increases the resolution to 0.5° × 0.5°. The domain is completed by the global layer whose resolution is 1.8° in longitude and 1° in latitude. This configuration does not require additional specification of horizontal boundary conditions in the regional domain (Deng et al., 2021; Meng et al., 2015), a clear advantage compared to other regionalized simulations.

Although the domain of interest for this simulation is in the mid-latitudes, the relative magnitude of ionospheric perturbations is highly dependent on the background electron density distribution, therefore the IMF and solar wind conditions from OMNI-web are utilized to drive GITM-R run for ~8 hr prior to the addition of a volcanic perturbation, to better specify the background state. The other input is solar irradiance given by an f10.7 index with value of 155 sfu. GITM-R's vertical extent covers from 100 to 600 km altitude. At the upper boundary an open condition is used in all layers. During the volcanic event, the lower boundary of the innermost domain is specified using the linear theory of AGW propagation, details of which are in Section 3.3 and Appendix A.

3.3. Source Representation and Propagation to 100 km

The atmospheric forcing for a particular volcanic eruption with mass injection rate given by $F_M(t)$ can be estimated, in the linear theory, by convolution with the atmosphere's response to a step function mass injection (Kanamori et al., 1994). In this model, the atmosphere's response is represented as a single point pressure oscillation described by Equation 1 (Kanamori, 2004; Kanamori et al., 1994).

$$p'(t) = Ae^{\frac{-1}{2H_\rho}}\left\{\delta(t-t_0) - \frac{\omega_a t_0 J_1\left[\omega_a\left(t^2-t_0^2\right)^{1/2}\right]}{\left(t^2-t_0^2\right)^{1/2}}H(t-t_0)\right\} \quad (1)$$

Here, A is meant to represent a kind of minimum impulse mass injection rate estimated for the first eruption phase as ~6.0e6 kg/s/m (Van Eaton et al., 2016), H_ρ is the local density scale height (~6 km), δ is the Dirac delta

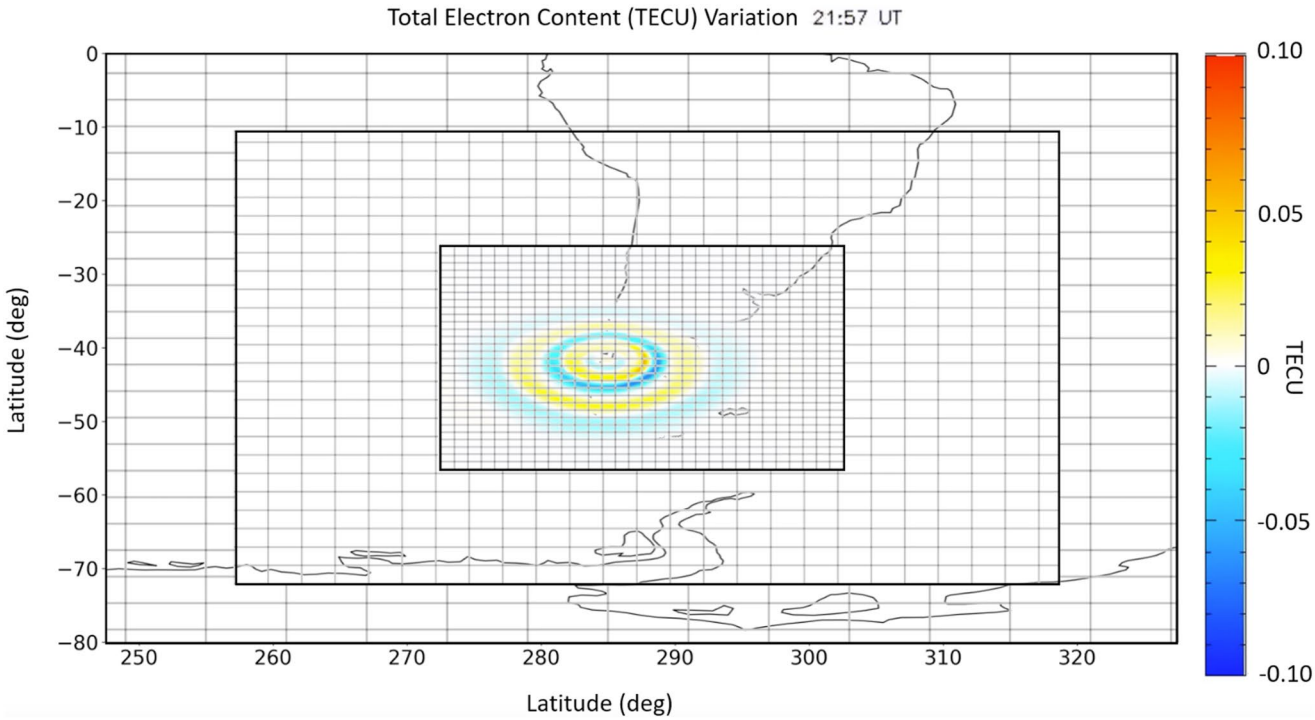

Figure 3. Example of GITM-R run with locally refined domain in the center. Red triangle is Calbuco location. Grid lines are displayed (light gray).

function, H is the Heaviside step function, J_1 is Bessel's function of the first kind (of order 1), ω_a is the (local) acoustic cut-off frequency (2.9 mHz, ~5.75 min), and t_0 is the eruption start time. The above equation is meant to represent the local solution of an isothermal atmosphere to a step change of mass injection. As in previous studies, the time series of the mass injection is represented as a Gaussian (derivative) shown in the equation below.

$$F_M(t) = B(t - t_0)e^{\frac{-(t-t_0)^2}{2\sigma_t^2}} \tag{2}$$

where B is an arbitrary factor used to adjust the magnitude of the final forcing signal for a comparable dTEC magnitude, and σ_t is some characteristic time of the eruption chosen here to be 58.5 s corresponding to a width at half maximum of approximately 4–6 min. The final forcing signal is created by the convolution of the assumed pressure response of system (1) and the event specific mass injection rate (2), $p' * F_M$ (Kanamori, 2004; Kanamori et al., 1994). In the future this framework would allow studies of specific volcanic events by using data to constrain the mass injection rate, but no such data was available for the Calbuco event. The normalized spectrum of the final forcing function is shown in Figure 4.

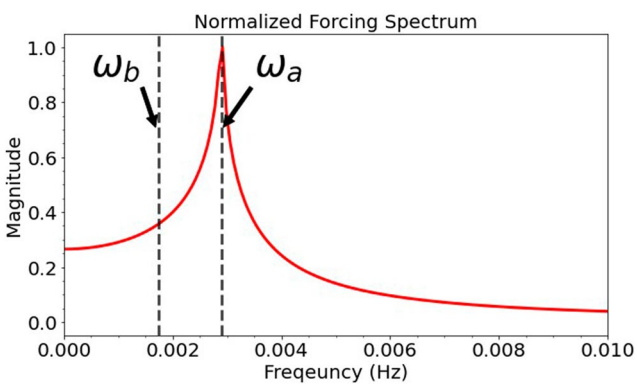

Figure 4. Normalized forcing spectrum showing clear spectral peak at local acoustic cut-off frequency. Dashed lines mark the local acoustic and buoyant frequencies.

The forcing function is then propagated to GITM-R's 100 km boundary using two different assumptions. First, Direct Spherical (DS) propagation utilizes the assumptions in Meng et al. (2015, 2018, 2022) to relate the horizontal and vertical structures as shown below,

$$k^2 = m^2 \tan^2 \theta. \tag{3}$$

where (k, m) are, respectively, the horizontal and vertical wavenumbers and θ is the propagation angle measured from a vertical axis extending from the source. This is meant to represent primary waves that directly propagate to the point of interest. To test the hypothesis that the second wave packet is evidence of local forcing due to ground-coupled airwaves, a second set of assumptions representing Ground Coupled (GC) propagation was also

introduced to slightly alter the propagation methodology. Instead of making an assumption on the horizontal track wavenumber $\boldsymbol{k}$, an assumption is made on the horizontal track phase speed $\left(\boldsymbol{v}_s = \frac{\omega}{\boldsymbol{k}} \right)$ following (Kurokawa & Ichihara, 2020) as

$$v_s = \frac{c_g}{\sin \theta_g}. \tag{4}$$

where $c_g = 334$ m/s is the sound speed along the ground, calculated by the MSIS profile and supported by infrasound records (Matoza et al., 2018), and θ_g is the ground strike angle measured from the vertical. Further details related to the equations used, definitions of the propagation and ground strike angle, as well as the reconstruction of the forcing to GITM's lower boundary are given in Appendix A. With the assumptions of Equations 3 or 4 the AGW dispersion relation (Equation A1) can be used to solve for the vertical wavenumber at a given frequency.

4. Results and Discussion

This section starts with Section 4.1 that discusses important features of the observations and potential explanations. In Section 4.2 the data is compared to GITM-R simulations of the first phase of the event driven by the DS and GC propagation assumptions discussed in Section 3/Appendix A. Shortfalls of the methodology and its relevance to recreation of the observed TEC signals are discussed in Section 4.3.

4.1. GNSS Observations

Focusing on the observations in the near-field (top left panel in Figure 1), the GNSS data (black line) shows at least two distinct wave packet structures; one occurring ~8–14 min after the eruption time and the other ~40–60 min after, suggesting these may be T1 and T2 disturbances respectively. Both wave packets are quasi-periodic with dominant modes between 4 and 6 mHz (with an overall maximum at ~4.67 mHz throughout the event; corresponding to a period of ~3.5–4 min) with the maximum magnitude of the detrended TEC being ~0.6 TECU, both of which are well supported by other studies (X. Liu et al., 2017; Shults et al., 2016). The magnitude of the second wave packet being larger than the first is an interesting observational result and may suggest indirect forcing caused by the eruption, such as turbulence/convection in the plume (Vadas & Liu, 2009; Vadas et al., 2003), leakage of concentrated energy due to atmospheric resonance (Watada & Kanamori, 2010), AGW interaction with the complicated topography of the Andes mountains such as diffracted infrasound (Le Pichon et al., 2002; Martire et al., 2022), or the breaking of mountain waves (Vadas et al., 2019) as a primary cause.

Missing from previous publications is the low frequency TID shown in the far-field response to the first eruption (top right panel, Figure 1). The analysis shows that the TEC signal becomes dominated by a spectral peak at ~0.8–0.9- mHz (~17–20 min). The high-frequency acoustic perturbations are modulated by the low frequency disturbance and reach magnitudes of 0.1–0.3 TECU. This mode might have been left out of the previous analysis because the filtering techniques in either instance use a bandpass approach with a lower cutoff frequency of 3 mHz. It is not uncommon for such a mode to follow acoustic dominated forcings, such as volcanos and earthquakes, and multiple low-frequency TIDs have been identified in the hours succeeding main eruption phases (De Angelis et al., 2011; Matsumura et al., 2011; Ripepe et al., 2010; Yue et al., 2022). However, the timing of this event coincides with the passage of the solar terminator (ST) line, as shown by the (black) dashed vertical line in the data panels for the first eruption phase in Figure 1, and caution must be taken when tracing the origin of this mode. If the ST wave (STW) plays a role, it may be expected that the near and far field observations (Forbes et al., 2008) should be similarly affected, however the near-field observations seem to be less influenced by the low frequency disturbance. The observed distribution perhaps suggests propagation from a localized source rather than thermal forcing induced by the terminator.

Meanwhile, geomagnetic storms can trigger TIDs propagating from high-latitudes to the middle- and low-latitudes (Lyons et al., 2019; Sheng et al., 2020; S.-R. Zhang, Nishimura, et al., 2022; Zhang, Vierinen, et al., 2022; K. Zhang et al., 2022; Zhu et al., 2022) and may be responsible for the low frequency mode. Although no noticeable storm/substorm can be identified from the Dst index during the Calbuco volcanic event, the detrended TEC shows several TIDs propagating both equatorward and poleward in the hours preceding the eruption. In our methodology, we acknowledge this mode's existence and explore the possibility of it being a low frequency (gravity mode)

CVID. We later supplement this view in the comparison to GITM-R simulation (Section 4.2) but suggest the reader to be aware of other possibilities.

Most of the results displayed for the second eruption phase (bottom half, Figure 1) are in the mid-field (~400–500 km) from the source. Notably, the GNSS data for the second phase mostly consist of only one distinct quasi-periodic wave packet that occurs ~40–60 min after the eruption time, a clear T2 type disturbance (Astafyeva, 2019; Shults et al., 2016). Although the eruption in the lower atmosphere lasted nearly 6 hr the upper atmosphere's response only lasts ~1.5 hr, like the first phase. Similarly, the dominant spectral content of the wave packet is nearly identical to the first eruption phase with most energy concentrated into the 4–6 mHz range. It is interesting to note the change in maximum dominant mode associated with PRN 13 opposed to PRN 28 suggesting the direction of IPP trajectory in this case, moving nearly parallel and anti-parallel respectively, may play a role in the perceived maximum frequency. The TEC response only reached an overall maximum of ~0.2 TECU, which agrees with previous publications, but is smaller than that of the first phase. The primary difference in TECU magnitude between the two phases is likely the contrast of the electron number densities between the day side and night side (Shults et al., 2016). Absent in the TEC response of the second eruption phase is the gravity mode and initial acoustic wave packet, to which there are some possible explanations. First, it should be noted that the background neutral atmosphere, as well as the local temperature and wind changes caused by the first eruption phase, may play a significant role in the propagation of AGWs launched from the second eruption phase. In fact, observational imaging of mesospheric airglow from the second eruption phase shows the GW propagation to be altered N-NE of the volcano breaking its nearly concentric pattern (Astafyeva, 2019; Miller et al., 2015). It is known, by advection of the ash plume, that the average wind field was also directed to N-NE direction and could contribute to the filtering of the GW disturbance which eventually arrive in the ionosphere affecting GNSS observations (Heale & Snively, 2015; Vadas et al., 2009). Second, IPP trajectories may have been too far/close, at the relevant times, to capture the initial wave packet or GW disturbance, although the total coverage suggests this to be unlikely. Third, Calbuco started a new eruptive phase after 43 years, with little precursory activity, meaning the first eruptive phase had to generate an overpressure that split the surrounding earth to open a conduit (Castruccio et al., 2016; Shults et al., 2016). It is perhaps this component of the eruption that induced the initial acoustic wave packet. As such, the absence of these features may suggest a difference in the forcing relevant to the IT system between the two eruption phases. Similarly, the main TEC response in both phases might represent some indirect AGW forcing mechanism and be separate from the initial AGW packet and trailing GW mode. As of now, it is unclear as to why the second, more powerful, eruption phase did not exhibit a clear double packet structure or trailing GW disturbance like that of the first phase and the proposed explanations would require additional inquiry. Therefore, in our simulation efforts, we focus on the first eruption phase.

Focusing attention on Figure 2a, the estimated apparent phase speed from the travel time diagram is ~870 m/s and ~811–986 m/s for the first and second packet respectively. This is in close agreement with those reported by Shults et al. (~911/897 m/s) and Liu et al. (~800 m/s) using approximately the same assumption on the F_2 peak (270 km). At larger distances from the volcano, a lower frequency GW starts to dominate the filtered TEC response and has an estimated apparent phase speed of ~200–222 m/s. The apparent phase speed of ~222 m/s for the gravity mode may be larger than the proposed mesopause bottleneck (Vadas & Azeem, 2021; Vadas et al., 2019), suggesting the observation may be a secondary GW, if its origin is the lower atmosphere. However, interaction with the mean flow can shift phase speeds to higher values and primary waves with sufficiently large vertical wavelengths can tunnel through evanescent regions in the lower atmosphere (Heale et al., 2022; Walterscheid & Hecht, 2003). Numerical results that resolve the lower atmosphere's structure have shown primary waves can reach the thermosphere with phase speeds larger than the proposed bottleneck, even when the calculation accounts for non-isothermal conditions (Gavrilov & Kshevetskii, 2018; Heale et al., 2022).

In Figure 2b it is interesting to note the mild suppression of GW signatures in using the smaller sliding window. This allows better visibility of GW induced TID from 400 to 650 km and may suggest lower frequency components play more of a role at larger distances. Such is expected from the far-field response of relatively localized point sources (Kanamori et al., 1994; C. H. Liu & Yeh, 1971) and may provide support for the CVID hypothesis.

4.2. GITM-R Simulations and Data-Model Comparisons

For comparison with filtered GNSS observations, GITM-R dTEC is created by subtracting the vTEC of a base run (with no forcing) from the vTEC of a run with forcing. As a result, the GITM-R dTEC represents the perturbed

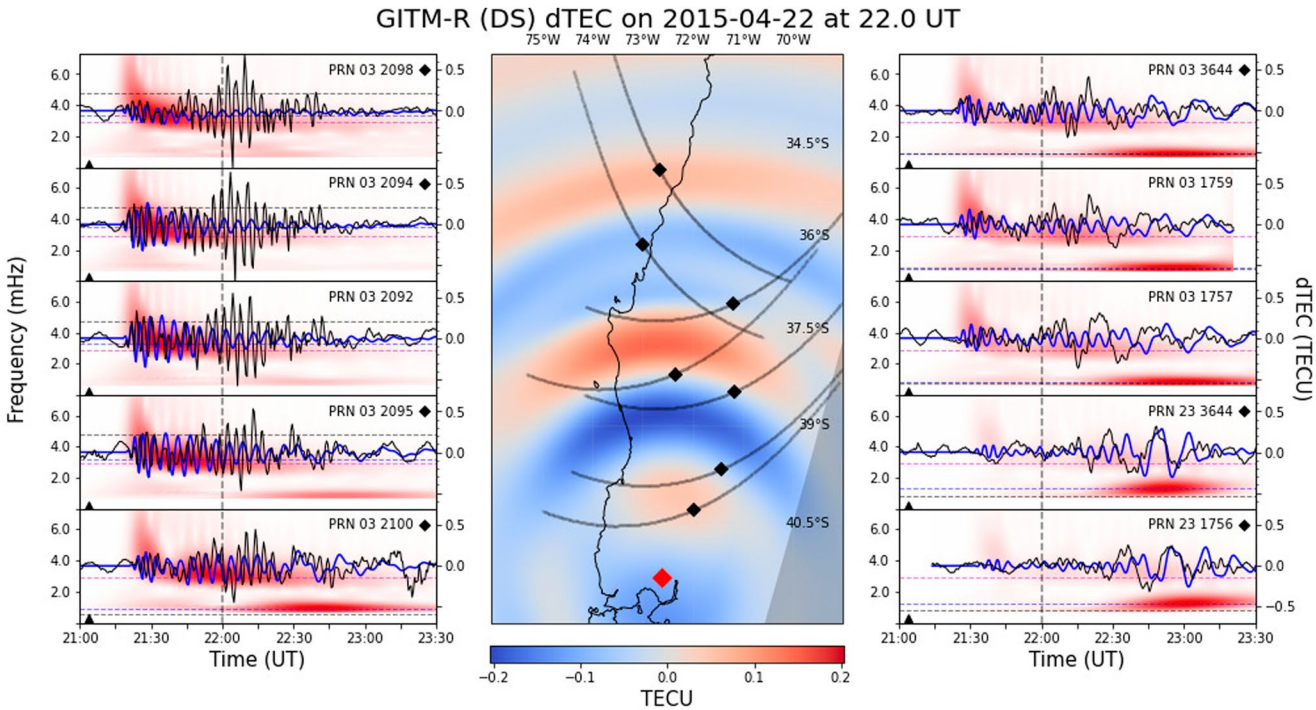

Figure 5. Direct comparison of simulated dTEC (blue) and GNSS observation (black) for the DP case. The format is the same as the top panel in Figure 1. The dashed magenta horizontal line represents the forcing frequency, while the dashed blue and black horizontal lines represent the frequency with maximum transform amplitude for GITM-R simulated and GNSS data time series respectively. The dashed vertical line represents the snapshot in time of the GITM-R simulated dTEC displayed as the color contour in the middle panel.

values and do not include the first order (linear) contributions of the ST wave. Only satellite-receiver pairs with elevation angles greater or equal to 40° were used in the analysis for comparison to GITM-R simulated vertical dTEC. Figure 5 shows the direct comparison of the GITM-R simulated dTEC (blue) and the filtered GNSS observation (black) along the satellite trajectories shown in Figure 1 under the direct spherical (DS) propagation assumption outlined in Section 3/Appendix A. The comparison shows decent agreement between simulation and observation for both acoustic and gravity perturbations. Arrival times and perturbation onsets in GITM-R match well to observation near the source but start to differ as the distance of the observations increases. Although the GITM-R dTEC magnitudes underpredict the observations near the source, and overpredict at larger distances, GITM-R reproduces the magnitude distribution as a function of radial distance from the source quite well. That is to say, GITM-R reproduces the general magnitude trend of first increasing then decreasing with distance. Additionally, the relative significance of the acoustic and gravity response is replicated, showing AGW dominant signature in the near-field and dominant GW signatures in far-field. The spectral results for the GITM-R simulation, displayed as the background contours of the left and right panels in Figure 5, show this distribution clearly as well.

The spectral analysis also shows that the initial wave packet's spectral content matches better to observation, showing dominance in 4–6 mHz range, but as the forcing continues the spectral content of the AGWs starts to approach closer to the forcing frequency (~2.9 mHz; 5.75 min), shown by the magenta dashed horizontal line in Figure 5. The (horizontal) dashed blue and black lines represent the spectral maximums found in the GITM-R simulated response and observational GNSS respectively. The initial agreement and later difference may explain why onset and phase of the initial wave packet match so well but start to differ significantly over time and will be further discussed in Section 4.3. Noticeable missing from the GITM-R results is the second wave packet in the acoustic mode that represents the main TEC response, although the overall timespan of the perturbation (~1.5–2 hr) seems to match well. As mentioned previously, the double wave packet structure is potentially an indication of dominant modes that together form an envelope in the TEC response. Although the forcing at any point along the lower boundary has two dominant modes (the acoustic forcing frequency and an additional gravity mode, dependent on the propagation angle and the chosen lower atmospheric value $[\overline{\omega}_b \, sin\, \theta]$), the current

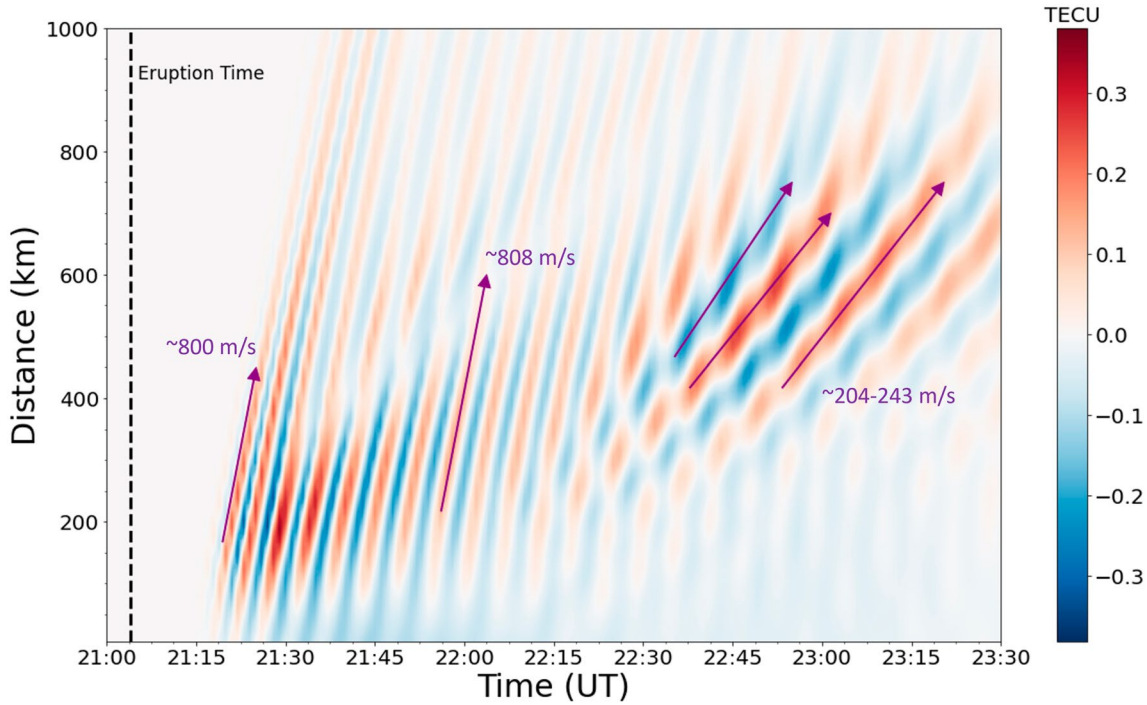

Figure 6. Recreated GITM-R dTEC travel time diagram for the DS case, showing approximated phase speeds.

specification is insufficient to recreate the 2-packet structure, because they are too separated in the frequency domain. However, this dominant gravity mode is mostly able to recreate the magnitude, phase, and timespan of the observed GW signatures found in the GNSS data, other than arrival offsets of ∼15–30 min and a more broadly defined spectral packet. Some satellite-receiver pairs find better agreement than others, both in apparent phase and magnitude for this mode. Pairs close to the source (left panel, Figure 5) match onset and magnitude of observations of the GW with good agreement, while others, such as those Northeast of the source (Top three right panels, Figure 5), are considerably smaller in magnitude and shifted ∼30 min in time. Interestingly, the farthest pairs (Bottom two right panels, Figure 5), have decent agreement with observations of the GW in magnitude and phase and only ∼15 min of offset.

The location-dependent performance may be due to an effect of the IPP trajectory motion, that is, in a direction nearly antiparallel to the GW, or suggest a different forcing mechanism than what is assumed. Meanwhile, the simplified propagation in the lower atmosphere (<100 km) will also contribute to the discrepancies in GW mode. For example, because the GITM simulated gravity mode is driven directly by the lower boundary forcing at ∼100 km altitude, the GW initial properties are strongly under the influence of the assumption of lower atmospheric background parameters. In the current approach the propagated GW signature is unaffected by atmospheric stratification and wind variations in the lower atmosphere, both of which may significantly alter propagation parameters, especially for low frequency waves (Heale & Snively, 2015; Vadas et al., 2003). Additionally, the primary forcing mechanism may not be the atmosphere's natural buoyant response, which the forcing is meant to represent, and instead be convectively generated in the plume (Vadas, 2013), produced by the dissipation of primary waves (Vadas, 2013; Vadas et al., 2009), result from thermal forcing near the solar terminator (Afraimovich, 2008; H. Liu et al., 2009; S. Zhang et al., 2021), or be TIDs propagating from unrelated sources.

Figure 6 is a GITM-R reproduction of the travel time diagram shown in Figure 2. To create the figure, a latitudinal slice is used extending from the volcano location. The AGW packet and trailing GW mode are clearly visible in the GITM-R results and have similar apparent phase speeds to the observations (Figure 2) equatorward of the volcano. The estimated equatorward phase speeds for simulated CVIDs associated with the first and second acoustic perturbations are ∼800 m/s (∼8% diff.) and ∼808 m/s (∼1%–18% diff.) respectively and the gravity wave perturbations are ∼204–243 m/s (∼2%–19% diff.). A proper comparison of simulated poleward phase speeds cannot be made due to lack of GNSS data coverage; however, the GITM-R results predict larger phase speeds for

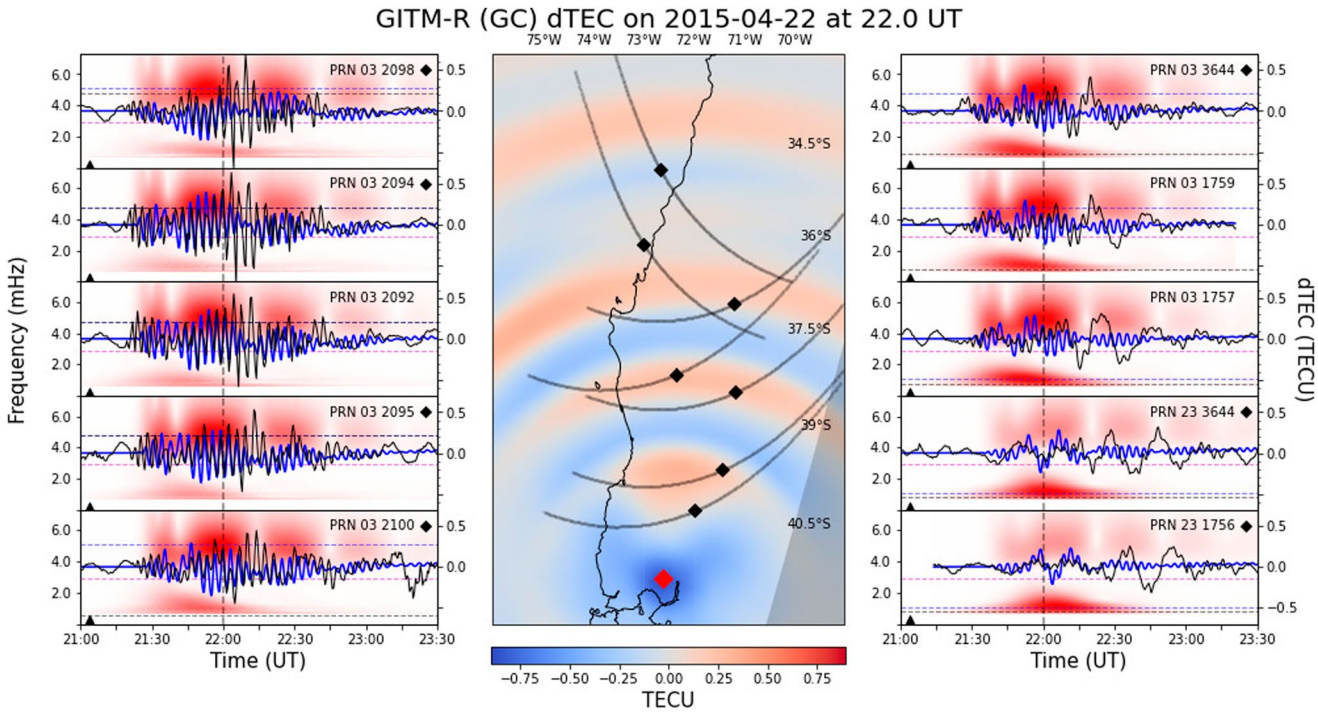

Figure 7. Direct comparison of simulated dTEC (blue) and GNSS observation (black) for the GC case. The format is identical to Figure 5.

the two modes (Figure not shown). The difference in simulated phase speeds equatorward/poleward of the source is likely related to the geomagnetic field orientation (Zettergren & Snively, 2015) or interaction of AGWs with the local neutral mean flow (Heale, et al., 2022). The GITM-R results also show a latitudinal asymmetry in the dTEC magnitude (not shown in Figure 6). A slight depletion occurs poleward most likely due to the downward transport of ions and electrons along magnetic field lines resulting in a higher recombination rate than plasma pushed equatorward (Meng et al., 2022).

Figure 7 shows a direct comparison of the GNSS data (black) and GITM-R simulated (blue) dTEC for the GC case, identical in format to Figures 1 and 5. Clearly noticeable in the simulated results is a multi-wave packet structure and tendency toward higher frequency modes in the range 4–6 mHz. While the initial wave packet is shifted by ∼10 min, the arrival time and phase of the second wave packet are in good agreement with GNSS observations. The duration of the second wave packet in GITM-R is shorter than observation and the associated peak perturbation is shifted ∼5 min. It is clear that the spectral content of the GITM-R results under the GC case matches better than the DS case, however the dominant modes in the GC case are still insufficient to recreate the exact TEC envelope. Far field AGW magnitudes agree with data and the lower frequency mode of ∼1 mHz starts to influence the acoustic signal upon arrival of the second wave packet but opposite in phase, shorter in duration, and smaller in magnitude to observation. This mode is not directly inputted along the lower boundary as forcing at 100 km altitude, as opposed to the DS case, because the low frequency modes ($\boldsymbol{\tau} > \boldsymbol{\tau}_a = 5.7$ min) are considered inefficient for coupling with the earth and left out of the reconstruction of the boundary condition (Godin et al., 2020). Instead, it appears that this mode is excited by the lower boundary forcing, in the lower thermosphere, and may be the model's buoyant response.

As seen in the snapshot displayed in the middle panels of Figures 5 and 7 the horizontal wavelength of the vdTEC in the GC case is shorter than that of the DS case due to the higher spectral content, as expected. The magnitude of the acoustic forcing directly above the vent appears to result in a TEC depletion in both specifications, shown in both the middle panel and in the closest displayed IPP comparison in Figures 5 and 7. It should be noted that this depletion appears much larger for the GC case than that of the DS case and could explain the sudden depletion found in PRN28 1770 in the second eruption phase (Figure 1). From the TTD of the GC case shown in Figure 8, the apparent phase speeds of the first acoustic wave packet is similar to the DS case (∼800 m/s, ∼8% diff) however the second wave packet is estimated faster (∼842 m/s) with a ∼4%–14% difference to observation.

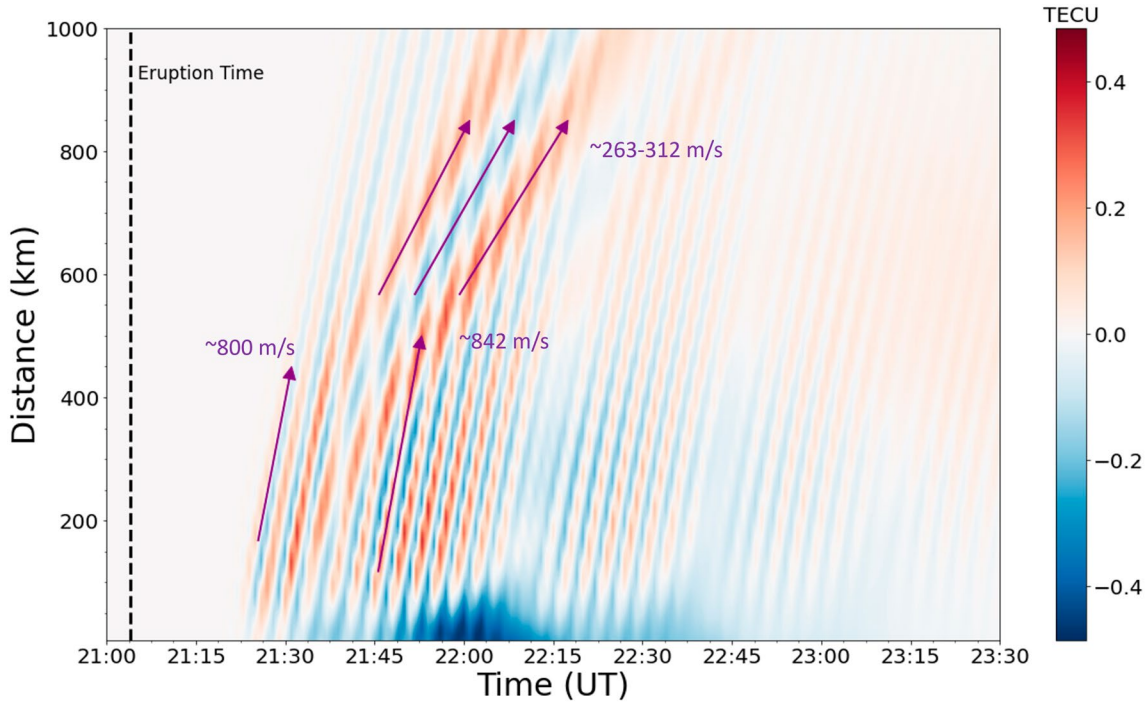

Figure 8. Recreated GITM-R dTEC travel time diagram for the GC case, showing approximated phase speeds.

The GW responses shown in Figure 8 have slightly different apparent phase speeds. The initial GW disturbance has the largest phase speed (∼312 m/s) while the second and third disturbance are slower at ∼285 and ∼263 m/s respectively. These estimates also suggest GW generation in the lower thermosphere (Vadas & Azeem, 2021), and the reduction of phase speed is also seen in other numerical simulations of acoustic forcing (Matsumura et al., 2011). These estimates yield ∼17%–44% diff. to the observational mode and might suggest the responsible mechanism is not the correct forcing of the observed GWs.

4.3. Discussion

The GITM-R simulations showed decent agreement with GNSS observations about the first acoustic wave packet and trailing gravity mode when using the DS propagation assumption to force the lower boundary. However, this specification of the forcing misses the second wave packet and its higher spectral content, whereas the GC case is in better agreement. Three shortcomings of the DS methodology may provide some explanation for these large differences. The first and most obvious being the oversimplification of the source representation. Our method is purposefully meant to resemble the natural acoustic mode response of the atmosphere in the vicinity of the volcano, however the true near field dynamics are certainly more complicated (Castruccio et al., 2016; Van Eaton et al., 2016). It is not qualitatively known what effect the near field complexity might have on the far-field response; however, the difference between the eruptive phases in the lower atmosphere contrasted with similarities in both waveform and spectral characteristics of the respective ionospheric responses provides evidence that a simplified source could be sufficient to describe the influence on the IT system, at least for this event. Second, the propagation to 100 km uses the assumption of a constant, windless atmosphere, and simplifying the dynamics similar to Meng et al. (2015). Our methodology would not include amplitude changes brought by partial reflection/transmission, tunneling, or doppler shifts associated with background winds (Balachandran, 1968; Brown & Sutherland, 2007; K. M. Huang et al., 2010). Therefore, the energy partitioning of the propagated signal may be over or underestimated for any given mode. Third, only the direct effect of the local atmosphere's average response is considered as the forcing in this simulation. Sudden changes in the atmospheric state are sure to produce broad spectral forcing and as such additional AGWs can be produced through secondary mechanisms dependent on the interactions between the volcano, atmosphere, and earth. For instance, convective systems can be formed from the cooling of injected gaseous material by the surrounding atmosphere, or as a response to an

atmospheric buoyant barrier (such as a temperature inversion layer) in general, and this can result in oscillatory forcing with various periods (Baines & Sacks, 2017). Additionally, the eruption will most likely generate some movement of the earth's surface, either internally or form airwaves impinging on the ground. While the earth and atmosphere have a large impedance, resonant coupling in the lower atmosphere is postulated to sustain amplitudes of long-duration acoustic wave trains as they propagate horizontally and has been used to explain infrasound, seismic, and TEC data related to various eruptions (Heki & Fujimoto, 2022; Matoza et al., 2018; Nakashima et al., 2016; Shults et al., 2016; Watada & Kanamori, 2010). These secondary coupling/generation mechanisms might provide an explanation for the delay in TEC response between T1 and T2 disturbances.

Shults et al. (2016) mentioned the spectral peaks of ∼3.8–5.2 mHz in the GNSS data are close to the periods of the first trapped atmospheric mode and its successive overtones. Additionally, Siemo-acoustic analysis of a collocated seismogram and infrasound station <1,000 km from the vent demonstrate a strong cross-correlation in their respective signals indicating air-ground coupling may play a significant role in the propagated air-waves (Matoza et al., 2018). Studies have shown for the coupled earth-atmosphere system that these modes are preferentially excited by above ground sources (Watada, 1995) and that the fundamental atmospheric acoustic mode ($_0P_{29}$) is nearly degenerate to that of the $_0S_{29}$ mode of the earth (with and eigen frequency of ∼3.7 mHz during July) (Kobayashi, 2007). These modes are reflected in the lower atmosphere due to the vertical temperature/wind structure and create resonance by forming standing wave patterns in the associated waveguides (Dautermann, Calais, & Mattioli, 2009; Godin, 2012; Godin et al., 2020; Lognonne et al., 1998, 2016; Watada, 1995). These waveguides can then efficiently leak energy into the thermosphere.

These studies form the basis for testing the GC specification, although the simplicity of our implementation, in comparison to those studies, cannot be neglected. Here, the vertical eigenfunction of the coupled system is not solved and instead an assumption is made on the horizontal trace velocity that relates to the atmospheric properties along the ground. In the limit that the ground strike angle approaches the horizontal, the horizontal dispersion approaches that of a pseudo-lamb wave propagating along earth's surface. It is important to note that pseudo-Lamb waves, in this context, refer to AGWs whose horizontal propagation is that of the Lamb wave but with a non-homogenous lower boundary condition, permitting non-hydrostatic solutions in the vertical ($w \neq 0$) (Walterscheid & Hecht, 2003). This distinction, between pseudo-Lamb and Lamb waves, may not be important when discussing observational data because the solution for the Lamb wave (from here on just LW) cannot be obtained in the general stratified environment without numerical computation (Godin, 2012). Theoretically, it's expected that spectrally broad LW packets can excite GWs in the lower thermosphere and may explain the GW modeling result shown in Figure 8 (Francis, 1973; Lindzen & Blake, 1972; Vadas, Becker, et al., 2023; Vadas, Figueiredo, et al., 2023; Walterscheid & Hecht, 2003; Watada, 1995). Vertical coupling of the Lamb wave, in a real atmosphere, is still not well understood and observational evidence of TIDs generated from LWs will have to be heavily supported by proper modeling to discern GWs generated by the passage of the LW (e.g., S.-R. Zhang, Nishimura, et al., 2022; Zhang, Vierinen, et al., 2022; K. Zhang et al., 2022) and GWs generated by the breaking of primary GWs (Vadas, Becker, et al., 2023; Vadas, Figueiredo, et al., 2023).

While the simplified approach outlined in this study was able to show some improvement in the data-model comparison it is clearly insufficient to reproduce some of the important features of the GNSS TEC data, such as the magnitude of the second wave packet. It is expected that including the vertical temperature structure below 100 km would allow for atmospheric resonance and not only increase the magnitude but help to partition the acoustic energy into dominant modes that produce a better agreement to the envelope of the two-packet structure found in the GNSS observations. A methodology with 2-way coupling of GITM-R and a lower atmosphere model might be needed to fully capture atmospheric resonance as some AGW propagation angles may result in turning point altitudes higher than the lower boundary of GITM (De Angelis et al., 2012; Le Pichon et al., 2002). Additional complexities such as coupling with solid earth might also improve the data-model comparison, due to the degeneracy of modes and the need for consistent lower boundary forcing as mentioned previously. It is likely, for a volcanic eruption, that atmospheric resonance occurs and is needed to fully explain the observed wavefield in the lower atmosphere but relevance to the IT system is still to be determined. Another potential candidate for formation and magnitude of the second wave packet is the complicated topography created by the Andes mountains just below the IPP trajectories to the east of the volcano. This topographical structure may induce significant interactions of the propagated air waves as mentioned previously (Fritts et al., 2021; Le Pichon et al., 2002; Martire et al., 2022; Vadas et al., 2019), and may also concentrate/diffract the coupled seismic waves to generate local enhancements/depletions of energy (Haney et al., 2009). Although many of these features are not included

in our current methodology, we believe this work provides a good starting point to further investigate the influence of the coupled earth-atmosphere on the IT system.

5. Conclusion

Observational GNSS TEC data was analyzed for both eruptive phases of the 2015 Calbuco event and it was shown that the magnitudes, duration, spectral content, and apparent phase speeds agree with previous publications of Shults et al. (2016) and X. Liu et al. (2017). By using a different TEC filtering technique, it was shown that the first phase has a notable difference in the observed IT response due to a far-field low frequency TID. While GW modes are expected in volcanic events, the timing and location, as well as the background TID activity, make it difficult to discern the TIDs origin without detailed modeling of both the source and other TID inducing ionospheric weather.

For our modeling approach, a simplified spectral model for spherical AGW propagation was used to force the lower boundary of a self-consistent 3D model for IT coupling, GITM-R. It was shown that GITM-R could reproduce important features of the observed GNSS data related to the sub-Plinian eruption of the first phase of the Calbuco 2015 event on April 22nd. In particular, GITM-R was able to reproduce the relative magnitude contributions of AGW perturbations as a function of radial distance, showing AW dominant perturbations near the source and GW dominant perturbations at further distances. The spectral results of the simulated initial acoustic perturbations were close to observation in the frequency domain, with dominance in the 4–6 mHz (2–4 min) range, while the majority of the AGWs in the timeseries are near the forcing frequency at ∼2.9 mHz (∼6 min). At later times and further distances, the simulated GW response has a spectral peak centered close to observation at ∼1 mHz (16–17 min) but was broader in spectral space. GITM-R's reproduction of the TTD also showed good agreement with estimated equatorward apparent phase speeds for either mode, with CVIDs associated with the acoustic and gravity wave perturbations having ∼4%–18% difference and ∼2%–19% difference, respectively.

Data-model comparisons were shown to improve when including the ground coupled (GC) specification, but the simplified propagation model was unable to predict relevant magnitudes unless an additional multiplicative factor ($q = 100$) was added. Most notably, the GC specification was able to reproduce the second, larger, wave packet (in the near field) and onset time, maintain spectral dominance in the acoustic range between 4 and 6 mHz, as in observations, and slightly improve estimated phase speeds of the acoustic wave packets. The overall TEC envelope in the observation is still not achieved, but the GC specification shows promise, and the results are expected to improve if the lower atmosphere is vertically resolved. Both specifications demonstrated lower frequency perturbations of ∼1–2 mHz in the far-field, however the ionospheric response for this mode is quite different because of the assumptions made in the lower boundary forcing. The GW packet response in the GC case had notable differences to the observed GW phase speeds with ∼17%–44% diff. and might suggest the generation mechanism did not play a significant role in the observed GW mode.

Comparison of the DS and GC cases suggests the initial wave packet might be acoustic waves propagating directly from the source while the second may be formed by the passage of a ground-coupled airwave. For the GW mode, the comparison shows distinct differences in TID propagation and characteristics from the different forcings however, the current forcing specification and modeling environment are not yet sufficient to comment on the origin of the GW mode shown in the GNSS observations. It is clear the current methodology needs to be improved in predicting travel time or phase variations for the GW mode as well as the AWs. A simple combination of the boundary conditions does not result in an improvement to the data-model comparisons, likely because of the difference in dominant modes between the two boundary forcings. Proper combination of the two specifications likely requires resolving the propagation changes induced by the atmosphere's vertical structure below 100 km.

Appendix A: Specification of GITM-R Lower Boundary Wave Forcing

As mentioned in the main text, GITM-R's lower boundary is at 100 km altitude and there is a need to represent the propagation of the forcing signal to the lower boundary. First, to represent the atmosphere below 100 km a local MSIS profile is used to calculate an altitudinal average of basic atmospheric properties. In our studies, $\overline{\rho}, \overline{T}$, and $\frac{d\overline{\rho}}{dz}$ are used to calculate $\overline{P}, \overline{c}^2, \overline{\omega}_a^2$, and $\overline{\omega}_b^2$. The purpose of this methodology is to skew the average

atmospheric properties to better represent important characteristics, such as $\overline{\omega}_a^2$ and $\overline{\omega}_b^2$, close to the vent altitude (~2 km). Dynamics of AGWs are represented using the linearized, density scaled, Euler equations in an isothermal (constant background) atmosphere in the absence of wind, shown below.

$$\frac{\partial \hat{\rho}}{\partial t} + \rho_0 \left(\nabla \cdot \hat{\boldsymbol{v}} - \frac{\imath \hat{w}}{2\overline{H}_\rho} \right) = 0$$

$$\frac{\partial \hat{u}}{\partial t} + \frac{1}{\rho_0} \frac{\partial \hat{P}}{\partial x} = 0$$

$$\frac{\partial \imath \hat{w}}{\partial t} + \frac{\overline{g}}{\rho_0} \hat{\rho} + \frac{1}{\rho_0} \left(\frac{\partial \hat{P}}{\partial z} - \frac{\hat{P}}{2\overline{H}_\rho} \right) = 0$$

$$\frac{\partial \hat{P}}{\partial t} - \overline{c}^2 \frac{\partial \hat{\rho}}{\partial t} + \rho_0 \beta \imath \hat{w} = 0$$

Where ρ_0 is the neutral density along the ground (~1.11 kg/m^3), $\overline{H}_\rho = -\frac{1}{\overline{\rho}} \frac{\overline{d\rho}}{dz}$, $\overline{c}^2 = \gamma R \overline{T}$, and $\beta = \frac{\overline{c}^2}{\overline{H}_\rho} - \overline{g}$. The equation set is formulated with $\hat{u}$ as a horizontal track velocity which can be generalized to three dimensions (Vadas & Nicolls, 2012). Taking the Fourier transform of the equation set ($\tilde{x} = \int \hat{x} e^{i(\omega t - \boldsymbol{k}\cdot\boldsymbol{r})} d\boldsymbol{r} dt$, $\boldsymbol{r} = (x, z)$, $\boldsymbol{k} = (k, m)$) gives the algebraic system,

$$\begin{bmatrix} i\omega^2 & -\rho_0 \alpha \omega & -ik^2 \\ \overline{g} & i\rho_0 \omega & -\alpha \\ -i\overline{c}^2 \omega & \rho_0 \beta & i\omega \end{bmatrix} \begin{bmatrix} \tilde{\rho} \\ \imath \tilde{w} \\ \tilde{p} \end{bmatrix} = 0$$

where $\alpha = im + \frac{1}{2H_\rho}$. The determinate of the above system, set to zero, gives the well know dispersion relation for AGWs where solving for the vertical wavenumber gives,

$$m^2 = \frac{\omega^2 - \overline{\omega}_a^2}{\overline{c}^2} - k^2 \frac{\omega^2 - \overline{\omega}_b^2}{\omega^2}. \tag{A1}$$

Here ω is the angular frequency, m is the vertical wavenumber, and k is the horizontal track wavenumber, and $\overline{\omega}_a^2 \equiv \frac{\overline{c}^2}{4\overline{H}_\rho^2}$, $\overline{\omega}_b^2 \equiv \frac{\overline{g}\beta}{\overline{c}^2}$ define the acoustic cut-off and buoyancy frequencies respectively. When $m^2 > 0$ the larger solution is used for acoustic frequencies ($\omega > \omega_a$) and the smaller solution for gravity frequencies ($\omega < \omega_b$) to give an upward propagating mode (Godin et al.. 2020; Watada, 2009). To use the dispersion relation and Fourier representation, the spectral method developed in Meng et al. (2015, 2018, 2022) is used to propagate the forcing spectrum using spherical waves under the assumption $k^2 = m^2 \tan^2 \theta$ where θ is the propagation angle measured from a vertical axis extending from the source. If $\boldsymbol{r} = (r_h, z - z_s)$ is the separation vector between any point along GITM-Rs lower boundary (x_b, y_b, z_b) and the source (x_s, y_s, z_s), then $\tan^2 \theta = \frac{r_h^2}{(z - z_s)}$ and Equation A1 can be used to calculate the vertical wavenumber. The AGW forcing to GITM-R is then given by spectral reconstructions

$$w = \left(\frac{\rho_{0km}}{\rho_{100km}} \right)^{1/2} \frac{1}{2\pi r} \int G_P^w \tilde{P} e^{i(\boldsymbol{k}\cdot\boldsymbol{r} - \omega t)} d\omega \tag{A2}$$

$$(u, v) = \left(\frac{\rho_0}{\rho_{100km}} \right)^{1/2} \frac{1}{2\pi r} \int \frac{(k_x, k_y)}{\rho_0 \omega} \tilde{P} e^{i(\boldsymbol{k}\cdot\boldsymbol{r} - \omega t)} d\omega \tag{A3}$$

$$T = \left(\frac{\rho_{0km}}{\rho_{100km}} \right)^{1/2} \frac{1}{2\pi r} \int \frac{\left(1 - \overline{T} R G_P^\rho\right)}{\rho_0 R} \tilde{P} e^{i(\boldsymbol{k}\cdot\boldsymbol{r} - \omega t)} d\omega \tag{A4}$$

where $\tilde{P}$ is the Fourier transform of the forcing signal, r is the separation vector between the source and the boundary point of interest, $\boldsymbol{k} = (|m|\tan\theta, m)$ is the assumed resonant k-vector for the given point, and G_P^w and G_p^ρ are the solutions to

$$\begin{bmatrix} i\omega^2 & -\rho_0\alpha\omega \\ \overline{g} & i\rho_0\omega \\ -i\overline{c}^{-2}\omega & \rho_0\beta \end{bmatrix} \begin{bmatrix} G_P^\rho \\ G_P^w \end{bmatrix} = \begin{bmatrix} ik^2 \\ \alpha \\ -i\omega \end{bmatrix}.$$

via left psudo-inverse. The Fourier decomposition/reconstruction is performed using 5,000 equally partitioned frequencies in the range [0, 40] mHz. The decomposition/reconstruction is done bin-wise using the non-integer generalized Goertzel algorithm (Sysel & Rajmic, 2012).

To test the hypothesis that the second wave packet is evidence of local forcing due to ground-coupled airwaves, the propagation methodology is slightly altered. Instead of making an assumption on the horizontal track wavenumber $\boldsymbol{k}$, an assumption is made on the horizontal track phase speed $\left(\boldsymbol{v}_s = \frac{\boldsymbol{\omega}}{\boldsymbol{k}}\right)$ following Kurokawa and Ichihara (2020) as

$$v_s = \frac{c_g}{\sin\theta_g}. \tag{A5}$$

where $c_g = 334$ m/s is the sound speed along the ground, calculated by the MSIS profile and supported by infrasound records (Matoza et al., 2018), and θ_g is the ground strike angle measured from the vertical. The strike angle θ_g is found for each angular frequency by first assuming direct propagation to the point $(r_h, -z_s)$, using the defined spatial structure, assuming downward energy propagation $(\frac{\partial\omega}{\partial m} < 0)$, to compute vertical and horizontal group velocities $\left(v_{gx} = \frac{\partial\omega}{\partial k}, v_{gz} = \frac{\partial\omega}{\partial m}\right)$, then calculating the radial separation between the ground strike point and the volcano's vent as $\boldsymbol{r_g} = \frac{-z_s v_{gx}}{v_{gz}}\hat{\boldsymbol{r}}_{\boldsymbol{h}}$. The strike angle can then be expressed as,

$$\theta_g = \sin^{-1}\left(\frac{r_g}{\sqrt{r_g^2 + z_s^2}}\right). \tag{A6}$$

Note as $r_g \gg z_s$, $\sin\theta_g \to 1$, and $v_s \to c_g$ representing a kind of Lamb mode. The desired changes come with an additional factor for dispersion under direct propagation to $(r_g, -z_s)$ defined as $\delta_s = \frac{e^{i\left(k_h r_g - m z_s\right)}}{\sqrt{r_g^2 + z_s^2}}$ where $\boldsymbol{k}$ is calculated on the direct propagation (DS) assumption and the denominator accounts for geometric spreading. An example for the reconstructed vertical velocity at GITM-R's lower boundary is,

$$w = \left(\frac{\rho_{0km}}{\rho_{100km}}\right)^{1/2} \frac{q}{2\pi} \int G_w^p \delta_s \tilde{P} e^{i[k\cdot(r-r_g)-\omega t]} d\omega$$

where the final magnitude is determined by a free parameter q. For the results displayed, q was chosen to give a comparable magnitude of the second wave packet ($q = 100$). Methodologically, a justification for this multiplicative factor can be made by assuming that very little leakage occurs without the occurrence of atmospheric resonance, noting that the current lower atmospheric methodology cannot support the phenomenon without resolving the vertical temperature profile (Godin et al., 2020). Preliminary calculations suggest a magnitude increase when considering thermal variation using the full MSIS profile, however a more in-depth treatment of atmospheric resonance is certainly needed rather than this simplified approach. Other contributing factors that have potential to increase the magnitude, and are not included in the current methodology, might include non-linear propagation affects, interaction with topography, or even the neutral dynamo as it is known the modes typically associated with atmospheric resonance have large energy densities near the E-region at ~80–120 km (Balachandran, 1968; Godin et al., 2020; Watada, 1995).

Data Availability Statement

The original GNSS observations were contributed by numerous community partners. The GNSS data and model outputs are available in S.-R. Zhang et al. (2023).

Acknowledgments
This work at UTA was supported by NASA through Grants 80NSSC20K1786, 80NSSC22K0061, 80NSSC20K0195, 80GSFC22CA011, and 80NSSC20K0606, and AFOSR through award FA9559-16-1-0364, FA9550-23-1-0634, and FA9550-23-1-0614. The authors acknowledge the Texas Advanced Computing Center (TACC, http://www.tacc.utexas.edu) at the University of Texas at Austin for providing HPC resources that have contributed to the research results reported within this paper. This research was supported by the International Space Science Institute (ISSI) for the international team on "Multi-Scale Magnetosphere-Ionosphere-Thermosphere Interaction." GNSS TEC data processing and CEDAR Madrigal open-access database are provided by the MIT Haystack Observatory under support from NSF geospace facility Grant AGS-1952737. SRZ acknowledges also funding from the AFOSR MURI Grant ONR15-FOA-0011, NSF Grants AGS-2033787 and AGS-2149698, NASA 80GSFC22CA011 and 80NSSC21K1310.

References

Aa, E., Zhang, S.-R., Erickson, P. J., Vierinen, J., Coster, A. J., Goncharenko, L. P., et al. (2022). Significant ionospheric hole and equatorial plasma bubbles after the 2022 Tonga volcano eruption. *Space Weather*, *20*(7), e2022SW003101. https://doi.org/10.1029/2022SW003101

Aa, E., Zhang, S.-R., Wang, W., Erickson, P. J., Qian, L., Eastes, R., et al. (2022). Pronounced suppression and X-pattern merging of equatorial ionization anomalies after the 2022 Tonga volcano eruption. *Journal of Geophysical Research: Space Physics*, *127*(6), e2022JA030527. https://doi.org/10.1029/2022JA030527

Afraimovich, E. L. (2008). First GPS-TEC evidence for the wave structure excited by the solar terminator. *Earth Planets and Space*, *60*(8), 895–900. https://doi.org/10.1186/BF03352843

Astafyeva, E. (2019). Ionospheric detection of natural hazards. *Reviews of Geophysics*, *57*(4), 1265–1288. https://doi.org/10.1029/2019RG000668

Astafyeva, E., Maletckii, B., Mikesell, T. D., Munaibari, E., Ravanelli, M., Coisson, P., et al. (2022). The 15 January 2022 Hunga Tonga eruption history as inferred from ionospheric observations. *Geophysical Research Letters*, *49*(10), e2022GL098827. https://doi.org/10.1029/2022GL098827

Bagiya, M. S., Sunil, A. S., Rolland, L., Nayak, S., Ponraj, M., Thomas, D., & Ramesh, D. S. (2019). Mapping the impact of non-tectonic forcing mechanisms on GNSS measured coseismic ionospheric perturbations. *Scientific Reports*, *9*(1), 18640. https://doi.org/10.1038/s41598-019-54354-0

Baines, P. G., & Sacks, S. (2017). The generation and propagation of atmospheric internal waves caused by volcanic eruptions. *Atmosphere*, *8*(3), 60. https://doi.org/10.3390/atmos8030060

Balachandran, N. K. (1968). Acoustic-gravity wave propagation in a temperature and wind-stratified atmosphere. *Journal of the Atmospheric Sciences*, *25*(5), 818–826. https://doi.org/10.1175/1520-0469(1968)025<0818:agwpia>2.0.co;2

Brown, G. L., & Sutherland, B. R. (2007). Internal wave tunnelling through non-uniformly stratified shear flow. *Atmosphere-Ocean*, *45*(1), 47–56. https://doi.org/10.3137/ao.v450104

Cahyadi, N. M., Handoko, Y. E., Rahayu, W. R., & Heki, K. (2021). Comparison of volcanic explosions in Japan using impulsive ionospheric disturbances. *Earth Planets and Space*, *73*(1), 228. https://doi.org/10.1186/s40623-021-01539-5

Cahyadi, N. M., Rahayu, R. W., Heki, K., & Nakashima, Y. (2020). Harmonic ionospheric oscillation by the 2010 eruption of the Merapi volcano, Indonesia, and the relevance of its amplitude to the mass eruption rate. *Journal of Volcanology and Geothermal Research*, *405*, 107047. https://doi.org/10.1016/j.jvolgeores.2020.107047

Calais, E., Minster, J. B., Hofton, M. A., & Hedlin, M. A. H. (1998). Ionospheric signature of surface mine blasts from global positioning system measurements. *Geophysical Journal International*, *132*(1), 191–202. https://doi.org/10.1046/j.1365-246x.1998.00438.x

Cappucci, M. (2021). Satellite captures La Palma volcano creating strange cloud ripple. Washington Post, Capital Weather Gang. https://www.washingtonpost.com/weather/2021/10/04/lapalma-volcano-cloud-waves-satellite/

Castruccio, A., Calvero, J., Segura, A., Samaniego, P., Olivier, R., Le Pennec, J., & Droguett, B. (2016). Eruptive parameters and dynamics of the April 2015 sub-Plinian eruptions of Calbuco volcano (southern Chile). *Bulletin of Volcanology*, *78*(9), 62. https://doi.org/10.1007/s00445-016-1058-8

Cheng, K., & Huang, Y. N. (1992). Ionospheric disturbances observed during the period of Mount Pinatubo eruptions in June 1991. *Journal of Geophysical Research*, *97*(A11), 16995–17004. https://doi.org/10.1029/92JA01462

Chimonas, G., & Hines, C. O. (1970). Atmospheric gravity waves launched by auroral currents. *Planetary and Space Science*, *18*(4), 565–582. https://doi.org/10.1016/0032-0633(70)90132-7

Dautermann, T., Calais, E., Lognonné, P., & Mattioli, G. S. (2009). Lithosphere-atmosphere-ionosphere coupling after the 2003 explosive eruption of the Soufrière Hills Volcano, Montserrat. *Geophysical Journal International*, *179*(3), 1537–1546. https://doi.org/10.1111/j.1365-246X.2009.04390

Dautermann, T., Calais, E., & Mattioli, G. S. (2009). Global Positioning System detection and energy estimation of the ionospheric wave caused by the 13 July 2003 explosion of the Soufrière Hills Volcano, Montserrat. *Journal of Geophysical Research*, *114*(B2), B02202. https://doi.org/10.1029/2008JB005722

De Angelis, S., Fee, D., Haney, M., & Schneider, D. (2012). Detecting hidden volcanic explosion from Mt. Cleveland Volcano, Alaska with infrasound and ground-coupled airwaves. *Geophysical Research Letters*, *39*(21), L21312. https://doi.org/10.1029/2012GL053635

De Angelis, S., McNutt, S. R., & Webley, P. W. (2011). Evidence of atmospheric gravity waves during the 2008 eruption of Okmok volcano from seismic and remote sensing observations. *Geophysical Research Letters*, *38*(10), L10303. https://doi.org/10.1029/2011GL047144

Deng, Y., Richmond, A. D., Ridley, A. J., & Liu, H.-L. (2008). Assessment of the non-hydrostatic effect on the upper atmosphere using a general circulation model (GCM). *Geophysical Research Letters*, *35*(1), L01104. https://doi.org/10.1029/2007GL032182

Deng, Y., & Ridley, A. J. (2014). Simulation of non-hydrostatic gravity wave propagation in the upper atmosphere. *Annales Geophysicae*, *32*(4), 443–447. https://doi.org/10.5194/angeo-32-443-2014

Deng, Y., Zhu, Q., Lin, C., Jin, M., Liu, C., & Sheng, C. (2021). Electric field variability and impact on the ionosphere-thermosphere. In Y. Nishimura, O. Verkhoglyadova, Y. Deng, & S. Zhang (Eds.), *Cross-scale coupling and energy transfer in the magnetosphere–ionosphere–thermosphere system*. Elsevier publication.

Forbes, J. M., Bruinsma, S. L., Miyoshi, Y., & Fujiwara, H. (2008). A solar terminator wave in thermosphere neutral densities measured by the CHAMP satellite. *Geophysical Research Letters*, *35*(14), L14802. https://doi.org/10.1029/2008GL034075

Francis, S. H. (1973). Acoustic-gravity modes and large-scale traveling ionospheric disturbances of a realistic, dissipative atmosphere. *Journal of Geophysical Research*, *78*(13), 2278–2301. https://doi.org/10.1029/JA078i013p02278

Fritts, D. C., Lund, T. S., Wan, K., & Liu, H. (2021). Numerical simulation of mountain waves over the southern Andes. Part II: Momentum fluxes and wave-mean-flow interactions. *Journal of the Atmospheric Sciences*, *78*(10), 3069–3088. https://doi.org/10.1175/JAS-D-200207.1

Gavrilov, N. M., & Kshevetskii, S. P. (2018). Features of the supersonic gravity wave penetration from the Earth's surface to the upper atmosphere. *Radiophysics Quantum Electronics*, *61*(4), 243–252. https://doi.org/10.1007/s11141-018-9885-4

Godin, O. A. (2012). Acoustic-gravity waves in atmospheric and oceanic waveguides. *Journal of the Acoustical Society of America*, *132*(2), 657–669. https://doi.org/10.1121/1.4731213

Godin, O. A., Zabotin, N. A., & Zabotin, L. (2020). Atmospheric resonances and their coupling to vibration of the ground and waves in the ocean. *Earth Planets and Space*, *72*(1), 125. https://doi.org/10.1186/s40623-020-01260-9

Haney, M. M., Wijk, K. V., Preston, L. A., & Aldridge, D. F. (2009). Observation and modeling of source effects in coda wave interferometry at Pavlof volcano. *The Leading Edge*, *28*(5), 554–560. https://doi.org/10.1190/1.3124930

Harding, B. J., Wu, Y.-J. J., Alken, P., Yamazaki, Y., Triplett, C. C., Immel, T. J., et al. (2022). Impacts of the January 2022 Tonga volcanic eruption on the ionospheric dynamo: ICON-MIGHTI and swarm observations of extreme neutral winds and currents. *Geophysical Research Letters*, *49*(9), e2022GL098577. https://doi.org/10.1029/2022GL098577

He, J., Astafyeva, E., Yue, X., Ding, F., & Maletckii, B. (2023). The giant ionospheric depletion on 15 January 2022 around the Hunga Tonga-Hunga Ha'apai volcanic eruption. *Journal of Geophysical Research: Space Physics*, *128*(1), e2022JA030984. https://doi.org/10.1029/2022JA030984

Heale, C. J., Inchin, P. A., & Snively, J. B. (2022). Primary versus secondary gravity wave responses at F-region heights generated by a convective source. *Journal of Geophysical Research: Space Physics*, *127*(1), e2021JA029947. https://doi.org/10.1029/2021JA029947

Heale, C. J., & Snively, J. B. (2015). Gravity wave propagation through a vertically and horizontally inhomogeneous background wind. *Journal of Geophysical Research: Atmospheres*, *120*(12), 5931–5950. https://doi.org/10.1002/2015JD023505

Heki, K. (2006). Explosion energy of the 2004 eruption of the Asama Volcano, central Japan, inferred from ionospheric disturbances. *Geophysical Research Letters*, *33*(14), L14303. https://doi.org/10.1029/2006GL026249

Heki, K., & Fujimoto, T. (2022). Atmospheric modes excited by the 2021 August eruption of the Fukutoku-Okanoba volcano, Izu-Bonin Arc, observed as harmonic TEC oscillations by QZSS. *Earth Planets and Space*, *74*(1), 27. https://doi.org/10.1186/s40623-022-01587-5

Heki, K., & Ping, J.-S. (2005). Directivity and apparent velocity of the coseismic ionospheric disturbances observed with a dense GPS array. *Earth and Planetary Science Letters*, *236*(3–4), 845–855. https://doi.org/10.1016/j.epsl.2005.06.010

Hines, C. O. (1960). Internal atmospheric gravity waves at ionospheric heights. *Canadian Journal of Physics*, *38*(11), 1441–1481. https://doi.org/10.1139/p60-150

Huang, C. Y., Helmboldt, J. F., Park, J., Pedersen, T. R., & Willemann, R. (2019). Ionospheric detection of explosive events. *Reviews of Geophysics*, *57*(1), 78–105. https://doi.org/10.1029/2017RG000594

Huang, K. M., Zhang, S. D., & Yi, F. (2010). Reflection and transmission of atmospheric gravity waves in a stably sheared horizontal wind field. *Journal of Geophysical Research*, *115*(D16), D16103. https://doi.org/10.1029/2009JD012687

Inchin, P. A. (2020). Atmospheric and ionospheric responses to acoustic and gravity waves driven by earthquakes and Tsunamis. Dissertations and Theses. *523*.

Kanamori, H. (2004). Some fluid-mechanical problems in geophysics—Waves in the atmosphere and fault lubrication. *Fluid Dynamics Research*, *34*(1), 1–19. https://doi.org/10.1016/j.fluiddyn.2003.08.006

Kanamori, H., Mori, J., & Harkrider, D. G. (1994). Excitation of atmospheric oscillations by volcanic eruptions. *Journal of Geophysical Research*, *99*(B11), 21947–21961. https://doi.org/10.1029/94JB01475

Klobuchar, J. A. (1985). Ionospheric time delay effects on earth space propagation. In A. S. Jursa (Ed.), *Handbook of geophysics and the space environment* (pp. 1084–1088). U.S. Air Force. Chapter 10.8.

Kobayashi, N. (2007). A new method to calculate normal modes. *Geophysical Journal International*, *168*(1), 315–331. https://doi.org/10.1111/j.1365-246X.2006.03220.x

Komjathy, A., Galvan, D. A., Stephens, P., Butala, M. D., Akopian, V., Wilson, B., et al. (2012). Detecting ionospheric TEC perturbations caused by natural hazards using a global network of GPS receivers: The Tohoku case study. *Earth Planets and Space*, *64*(12), 24–1294. https://doi.org/10.5047/eps.2012.08.003

Koucká Knížová, P., Laštovicka, J., Kouba, D., Mošna, Z., Podolská, K., Potužníková, K., et al. (2021). Ionosphere influenced from lower-lying atmospheric regions. *Frontiers in Astronomy and Space Sciences*, *8*, 651445. https://doi.org/10.3389/fspas.2021.651445

Kurokawa, K. A., & Ichihara, M. (2020). Identification of infrasonic and seismic components of tremors in single-station records: Application to the 2013 and 2018 events at Ioto Island, Japan. *Earth Planets and Space*, *72*(1), 171. https://doi.org/10.1186/s40623-020-01302

Lee, G. R., Gommers, R., Wasilewski, F., Wohlfahrt, K., & O'Leary, A. (2019). PyWavelets: A Python package for wavelet analysis. *Journal of Open Source Software*, *4*(36), 1237. https://doi.org/10.21105/joss.01237

Le Pichon, A., Guilbert, J., Vega, A., Garcés, M., & Brachet, N. (2002). Ground-coupled air waves and diffracted infrasound from the Arequipa earthquake of June 23, 2001. *Geophysical Research Letters*, *29*(18), 1886. https://doi.org/10.1029/2002GL015052

Lindstrom, S. (2015). *Gravity waves associated with Calbuco volcanic eruption*. CIMSS Satellite Blog, University of Wisconsisn-Madison. Retrieved from https://cimss.ssec.wisc.edu/satellite-blog/archives/18174

Lindzen, R. S., & Blake, D. (1972). Lamb waves in the presence of realistic distributions of temperature and dissipation. *Journal of Geophysical Research*, *77*(12), 2166–2176. https://doi.org/10.1029/JC077i012p02166

Liu, C. H., & Yeh, K. C. (1971). Excitation of acoustic-gravity waves in an isothermal atmosphere. *Tellus*, *23*(2), 150–163. https://doi.org/10.3402/tellusa.v23i2.10375

Liu, H., Lu¨hr, H., & Watanabe, S. (2009). A solar terminator wave in thermospheric wind and density simultaneously observed by CHAMP. *Geophysical Research Letters*, *36*(10), L10109. https://doi.org/10.1029/2009GL038165

Liu, L., Morton, Y. J., Cheng, P.-H., Amores, A., Wright, C. J., & Hoffmann, L. (2023). Concentric traveling ionospheric disturbances (CTIDs) triggered by the 2022 Tonga volcanic eruption. *Journal of Geophysical Research: Space Physics*, *128*(2), e2022JA030656. https://doi.org/10.1029/2022JA030656

Liu, X., Zhang, Q., Shah, M., & Hong, Z. (2017). Atmospheric-ionospheric disturbances following the April 2015 Calbuco volcano from GPS observations. *Advances in Space Research*, *60*(12), 2836–2846. https://doi.org/10.1016/j.asr.2017.07.007

Lognonné, P., Clévédé, E., & Kanamori, H. (1998). Computation of seismograms and atmospheric oscillation by normal-mode summation for a spherical earth model with realistic atmosphere. *Geophysical Journal International*, *135*(2), 388–406. https://doi.org/10.1046/j.1365-246x.1998.00665.x

Lognonné, P., Karakostas, F., Rolland, L., & Nishikawa, Y. (2016). Modeling of atmospheric-coupled Rayleigh waves on planets with atmosphere: From Earth observation to Mars and Venus perspectives. *Journal of the Acoustical Society of America*, *140*(2), 1447–1468. https://doi.org/10.1121/1.4960788

Lyons, L. R., Nishimura, Y., Zhang, S. R., Coster, A. J., Bhatt, A., Kendall, E., & Deng, Y. (2019). Identification of auroral zone activity driving large-scale traveling ionospheric disturbances. *Journal of Geophysical Research: Space Physics*, *124*(1), 700–714. https://doi.org/10.1029/2018JA025980

Manta, F., Occhipinti, G., Hill, E. M., Perttu, A., Assink, J., & Taisne, B. (2021). Correlation between GNSS-TEC and eruption magnitude supports the use of ionospheric sensing to complement volcanic hazard assessment. *Journal of Geophysical Research: Solid Earth*, *126*(2), e2020JB020726. https://doi.org/10.1029/2020JB020726

Martire, L., Martin, R., Brissaud, Q., & Garcia, R. F. (2022). SPECFEM2D-DG, an open-source software modelling mechanical waves in coupled solid–fluid systems: The linearized Navier–Stokes approach. *Geophysical Journal International*, *228*(1), 664–697. https://doi.org/10.1093/gji/ggab308

Matoza, R. S., Fee, D., Assink, J. D., Iezzi, A. M., Green, D. N., Kim, K., et al. (2022). Atmospheric waves and global seismoacoustic observations of the January 2022 Hunga Tonga eruption. *Science*, *377*(6601), 95–100. https://doi.org/10.1126/science.abo7063

Matoza, R. S., Fee, D., Green, D. N., Le Pichon, A., Vergoz, J., Haney, M. M., et al. (2018). Local, regional, and remote seismo-acoustic observations of the April 2015 VEI 4 eruption of Calbuco volcano, Chile. *Journal of Geophysical Research: Solid Earth*, *123*(5), 3814–3827. https://doi.org/10.1002/2017JB015182

Matsumura, M., Saito, A., Iyemori, T., Shinagawa, H., Tsugawa, T., Otsuka, Y., et al. (2011). Numerical simulations of atmospheric waves excited by the 2011 of the Pacific coast of Tohoku Earthquake. *Earth Planets and Space*, *60*, 885–889.

Meng, X., Komjathy, A., Verkhoglyadova, O. P., Yang, Y.-M., Deng, Y., & Mannucci, A. J. (2015). A new physics-based modeling approach for tsunami-ionosphere coupling. *Geophysical Research Letters*, *42*(12), 4736–4744. https://doi.org/10.1002/2015GL064610

Meng, X., Ravanelli, M., Komjathy, A., & Verkhoglyadova, O. P. (2022). On the north-south asymmetry of co-seismic ionospheric disturbances during the 16 September 2015 Illapl M8.3 earthquake. *Geophysical Research Letters*, *49*(8), e2022GL098090. https://doi.org/10.1029/2022GL098090

Meng, X., Verkhoglyadova, O. P., Komjathy, A., Savastano, G., & Mannucci, A. J. (2018). Physics-based modeling of earthquake-induced ionospheric disturbances. *Journal of Geophysical Research: Space Physics*, *123*(9), 8021–8038. https://doi.org/10.1029/2018JA025253

Miller, D. S., Straka, W. C., III., Jia, Y., Smith, M. S., Alexander, J. M., Hoffmann, L., et al. (2015). Upper atmospheric gravity wave details revealed in nightglow satellite imagery. *Proceedings of the National Academy of Sciences of the United States of America*, *112*(49), E6728–E6735. https://doi.org/10.1073/pnas.1508084112

Nakashima, Y., Heki, K., Takeo, A., Cahyadi, N. M., Aditiya, A., & Yoshizawa, K. (2016). Atmospheric resonant oscillations by the 2014 eruption of the Kelud volcano, Indonesia, observed with the ionospheric total electron contents and seismic signals. *Earth and Planetary Science Letters*, *434*, 112–116. https://doi.org/10.1016/j.epsl.2015.11.029

Ridley, A. J., Deng, Y., & Tóth, G. (2006). The global ionosphere–thermosphere model. *Journal of Atmospheric and Solar-Terrestrial Physics*, *68*(8), 839–864. https://doi.org/10.1016/j.jastp.2006.01.008

Ripepe, M., De Angelis, S., Lacanna, G., & Voight, B. (2010). Observation of infrasonic and gravity waves at Soufrière Hills Volcano, Montserrat. *Geophysical Research Letters*, *37*(19), L00E14. https://doi.org/10.1029/2010GL042557

Sheng, C., Deng, Y., Zhang, S.-R., Nishimura, Y., & Lyons, L. R. (2020). Relative contributions of ion convection and particle precipitation to exciting large-scale traveling atmospheric and ionospheric disturbances. *Journal of Geophysical Research: Space Physics*, *125*(2), e2019JA027342. https://doi.org/10.1029/2019JA027342

Shults, K., Astafyeva, E., & Adourian, S. (2016). Ionospheric detection and localization of volcano eruptions on the example of the April 2015 Calbuco events. *Journal of Geophysical Research: Space Physics*, *121*(10), 10303–10315. https://doi.org/10.1002/2016JA023382

Sysel, P., & Rajmic, P. (2012). Goertzel algorithm generalized to non-integer multiples of fundamental frequency. *EURASIP Journal on Applied Signal Processing*, *2012*(1), 56. https://doi.org/10.1186/1687-6180-2012-56

Themens, D. R., Watson, C., Žagar, N., Vasylkevych, S., Elvidge, S., McCaffrey, A., et al. (2022). Global propagation of ionospheric disturbances associated with the 2022 Tonga volcanic eruption. *Geophysical Research Letters*, *49*(7), e2022GL098158. https://doi.org/10.1029/2022GL098158

Vadas, S. L. (2013). Compressible *f*-plane solutions to body forces, heatings, and coolings, and application to the primary and secondary gravity waves generated by a deep convective plume. *Journal of Geophysical Research: Space Physics*, *118*(5), 2377–2397. https://doi.org/10.1002/jgra.50163

Vadas, S. L., & Azeem, I. (2021). Concentric secondary gravity waves in the thermosphere and ionosphere over the continental United States on 25-26 march 2015 from deep convection. *Journal of Geophysical Research: Space Physics*, *126*(2), e2020JA028275. https://doi.org/10.1029/2020JA028275

Vadas, S. L., Becker, E., Figueiredo, C., Bossert, K., Harding, B. J., & Gasque, L. C. (2023). Primary and secondary gravity waves and large-scale wind changes generated by the Tonga volcanic eruption on 15 January 2022: Modeling and comparison with ICON-MIGHTI winds. *Journal of Geophysical Research: Space Physics*, *128*(2), e2022JA031138. https://doi.org/10.1029/2022JA031138

Vadas, S. L., Figueiredo, C., Becker, E., Huba, J. D., Themens, D. R., Hindley, N. P., et al. (2023). Traveling ionospheric disturbances induced by the secondary gravity waves from the Tonga eruption on 15 January 2022: Modeling with MESORAC/HIAMCM/SAMI3 and comparison of GPS/TEC and ionosonde data. *Journal of Geophysical Research: Space Physics*, *128*, e2023JA031408. https://doi.org/10.1029/2023JA031408

Vadas, S. L., Fritts, D. C., & Alexander, M. J. (2003). Mechanism for the generation of secondary waves in wave breaking regions. *Journal of the Atmospheric Sciences*, *60*(1), 194–214. https://doi.org/10.1175/1520-0469(2003)060<0194:mftgos>2.0.co;2

Vadas, S. L., & Liu, H. L. (2009). Generation of large scale gravity waves and neutral winds in the thermosphere from the dissipation of convectively generated gravity waves. *Journal of Geophysical Research*, *114*(A10), A10310. https://doi.org/10.1029/2009ja014108

Vadas, S. L., & Nicolls, M. J. (2012). The phases and amplitudes of gravity waves propagating and dissipating in the thermosphere: Theory. *Journal of Geophysical Research*, *117*(A5), A05322. https://doi.org/10.1029/2011JA017426

Vadas, S. L., Xu, S., Yue, J., Bossert, K., Becker, E., & Baumgarten, G. (2019). Characteristics of the quiet-time hot spot gravity waves observed by GOCE over the southern Andes on 5 July 2010. *Journal of Geophysical Research: Space Physics*, *124*(8), 7034–7061. https://doi.org/10.1029/2019JA026693

Vadas, S. L., Yue, J., She, C.-Y., Stamus, P. A., & Liu, A. Z. (2009). A model study of the effects of winds on concentric rings of gravity waves from a convective plume near Fort Collins on 11 May 2004. *Journal of Geophysical Research*, *114*(D6), D06103. https://doi.org/10.1029/2008JD01

Van EatonAmigo, A. R. A., Bertin, D., Mastin, L. G., Giacosa, R. E., Gonzalez, J., Valderrama, O., et al. (2016). Volcanic lightning and plume behavior reveal evolving hazards during the April 2015 eruption of Calbuco volcano, Chile. *Geophysical Research Letters*, *43*(7), 3563–3571. https://doi.org/10.1002/2016GL068076

Virtanen, P., Gommers, R., Oliphant, T. E., Haberland, M., Reddy, T., Cournapeau, D., et al. (2020). SciPy 1.0: Fundamental algorithms for scientific computing in Python. *Nature Methods*, *17*(3), 261–272. https://doi.org/10.1038/s41592-019-0686-2

Walterscheid, R. L., & Hecht, J. H. (2003). A reexamination of evanescent acoustic-gravity waves: Special properties and aeronomical significance. *Journal of Geophysical Research*, *108*(D11), 4340. https://doi.org/10.1029/2002JD002421

Watada, S. (1995). Part I: Near-source acoustic coupling between the atmosphere and the solid Earth during volcanic eruptions. (Thesis). California Institute of Technology.

Watada, S. (2009). Radiation of acoustic and gravity waves and propagation of boundary waves in the stratified fluid from a time-varying bottom boundary. *Journal of Fluid Mechanics*, *627*, 361–377. https://doi.org/10.1017/S0022112009005953

Watada, S., & Kanamori, H. (2010). Acoustic resonant oscillations between the atmosphere and the solid Earth during the 1991 Mt. Pinatubo eruption. *Journal of Geophysical Research*, *115*(B12), B12319. https://doi.org/10.1029/2010JB007747

Yue, J., Miller, S. D., Straka, W. C., III., Noh, Y.-J., Chou, M.-Y., Kahn, R., & Flower, V. (2022). La Soufriere volcanic eruptions launched gravity waves into space. *Geophysical Research Letters*, *49*(8), e2022GL097952. https://doi.org/10.1029/2022GL097952

Zettergren, M. D., & Snively, J. B. (2015). Ionospheric response to infrasonic-acoustic waves generated by natural hazard events. *Journal of Geophysical Research: Space Physics*, *120*(9), 8002–8024. https://doi.org/10.1002/2015JA021116

Zhang, K., Wang, H., Zhong, Y., Xia, H., & Qian, C. (2022). The temporal evolution of F-region equatorial ionization anomaly owing to the 2022 Tonga volcanic eruption. *Remote Sensing*, *14*(22), 5714. https://doi.org/10.3390/rs14225714

Zhang, S., Erickson, P. J., Gasque, L. C., Aa, E., Rideout, W., Vierinen, J., et al. (2021). Electrified post sunrise ionospheric perturbations at Millstone Hill. *Geophysical Research Letters*, *48*(18), e2021GL095151. https://doi.org/10.1029/2021gl095151

Zhang, S.-R., Deng, Y., & Tyska, J. (2023). GNSS and GITM-R outputs for "ionospheric disturbances generated by the 2015 Calbuco eruption: Comparison of GITM-R simulations and GNSS observations" [Dataset]. Zenodo. https://doi.org/10.5281/zenodo.7787345

Zhang, S.-R., Erickson, P. J., Goncharenko, L. P., Coster, A. J., Rideout, W., & Vierinen, J. (2017). Ionospheric bow waves and perturbations induced by the 21 August 2017 solar eclipse. *Geophysical Research Letters*, *44*(24), 12067–12073. https://doi.org/10.1002/2017GL076054

Zhang, S.-R., Nishimura, Y., Erickson, P. J., Aa, E., Kil, H., Deng, Y., et al. (2022). Traveling ionospheric disturbances in the vicinity of storm-enhanced density at midlatitudes. *Journal of Geophysical Research: Space Physics*, *127*(8), e2022JA030429. https://doi.org/10.1029/2022ja030429

Zhang, S.-R., Vierinen, J., Aa, E., Goncharenko, L. P., Erickson, P. J., Rideout, W., et al. (2022). 2022 Tonga volcanic eruption induced global propagation of ionospheric disturbances via Lamb waves. *Frontiers in Astronomy and Space Sciences*, *9*, 871275. https://doi.org/10.3389/fspas.2022.871275

Zhao, Y., Deng, Y., Wang, J., Zhang, S., & Lin, C. (2020). Tropical cyclone induced gravity wave perturbations in the upper atmosphere: GITM-R simulations. *Journal of Geophysical Research: Space Physics*, *125*(7), e2019JA027675. https://doi.org/10.1029/2019JA027675

Zhu, Q., Lu, G., & Deng, Y. (2022). Low and mid-latitude ionospheric response to the 2013 St. Patrick's Day geomagnetic storm in the American sector: Global ionosphere thermosphere model simulation. *Frontiers in Astronomy and Space Sciences*, *9*, 916739. https://doi.org/10.3389/fspas.2022.916739